

Simeon ZHYLA¹, Valerii VOLOSUYUK¹, Vladimir PAVLIKOV¹,
Nikolay RUZHENTSEV¹, Eduard TSERNE¹, Anatoliy POPOV¹,
Oleksandr SHMATKO¹, Olena HAVRYLENKO¹, Nataliia KUZMENKO²,
Kostiantyn DERGACHOV¹, Yuliya AVERYANOVA², Olga SUSHCHENKO²,
Maksym ZALISKYI², Oleksandr SOLOMENTSEV², Ivan OSTROUMOV²,
Borys KUZNETSOV³, Tatyana NIKITINA⁴

¹ National Aerospace University “Kharkiv Aviation Institute”, Kharkiv, Ukraine

² National Aviation University, Kyiv, Ukraine

³ State Institution “Institute of Technical Problems of Magnetism
of the National Academy of Sciences of Ukraine”, Kharkiv, Ukraine

⁴ Kharkiv National Automobile and Highway University, Kharkiv, Ukraine

PRACTICAL IMAGING ALGORITHMS IN ULTRA-WIDEBAND RADAR SYSTEMS USING ACTIVE APERTURE SYNTHESIS AND STOCHASTIC PROBING SIGNALS

The **subject** of the manuscript is the algorithms for radar imaging. This research develops imaging methods and algorithms for wideband and ultrawideband active aperture synthesis systems with antenna arrays and stochastic probing signals. The use of antenna arrays makes it possible to obtain radar images without the need to move radar or antenna system in space. The use of wideband and ultra-wideband stochastic probing signals is justified by their narrow autocorrelation functions. This increased the resolution of the obtained images. The main **idea** of the proposed algorithms is to filter the original wideband signal into several narrowband processes. Furthermore, only the central frequencies of each narrowband signal were processed. This approach allows us to use the classical widespread methods of aperture synthesis for the case of a wideband signal. Usually, they are applicable only for narrowband signals that satisfy the condition of a quasi-monochromatic approximation. This significantly reduces the overall computational complexity of the imaging algorithm, which simplifies its further practical implementation on the existing radioelement base. Because of the simulation, a primary radar image has been obtained and the overall performance of the proposed approach to processing wideband signals has been confirmed. An increase in the quality of the obtained image when using a multiple of frequency ranges is shown. An experimental study of the effect of processing a wideband signal only at its centre frequency instead of the entire frequency band is conducted. During the experiment, the correlation functions of the signals received by two spaced receivers were obtained. As a result, the Van Cittert-Zernike theorem has been experimentally confirmed. It allows signal processing only at its centre frequency instead of the entire frequency band. Simultaneously, the prospect of expanding the bandwidth of the probing signal is indicated. It, in the presence of a wideband element base and devices for high-speed signal processing, will further increase the imaging resolution of a radar system.

Keywords: active aperture synthesis; radar imaging algorithms; wideband systems; correlation functions.

Introduction

Motivation. At present, to solve the problems of terrain mapping, air and space reconnaissance, and missile weapons control, Radar Systems (RS) based on aerospace vehicles are actively used [1, 2]. An important feature of such advanced systems is the use of underwing, under-fuselage and other types of Antenna Arrays (AA), as well as appropriate space-time signal processing [3, 4]. However, the operation algorithms of many existing RS provide for the processing of narrowband signals only. Latest advances in the radioelement

base field have made it possible to create systems with ultra-wideband signals space-time processing [5, 6]. Of particular interest in this area are the problems of spatially extended objects imaging using stochastic Ultra-WideBand (UWB) signals. Such signals in the form of stationary random processes have narrow correlation functions, which is important in radar imaging [7].

State of the Art. At the moment, synthetic aperture radars are the most effective among active RS [8]. The algorithm of their work consists in the coherent accumulation of signals during an aerospace carrier movement. In passive and radio astronomy RS operat-

ing with stochastic signals, aperture synthesis methods are actively used to form images [9, 10]. Often, such systems process signals received from sources of radio-thermal radiation. An important basis of RS with aperture synthesis is the using of effective observation area and the receiving signals by spatially distributed antenna systems [11].

The mentioned methods have certain differences. Passive systems do not always take into account the mutual motion of the radiation source and the area of its registration. However, of particular interest is the use of aperture synthesis methods for imaging by active radar stations. In this case, to increase the imaging resolution, it is advisable to use segments of noise-like wideband signals as probing ones. The use of systems with aperture synthesis is relevant for surface imaging from aerospace vehicles at probing angles close to nadir. This is due to the fact that classical side-looking and synthetic aperture radars cannot provide sufficient image resolution in these directions.

Currently, there are already some options for solving this problem. In this study [12], pointed the prospects of implementation of a multi-position satellite system for high-resolution radio imaging. Multi-positioning ensures global imaging. However, it does not allow to quickly surveying the given local areas of the surface, which is important when solving military tasks. Additionally, such systems cannot be implemented on one aerospace carrier, which significantly increases the cost of their deployment.

Some developers propose to use a spotlight survey of a given surface area [13, 14]. This ensures the radio imaging with high spatial resolution of a small surface area.

Another direction of research is the implementation of passive aperture synthesis methods taking into account the movement of the carrier [15, 16]. These research involve the processing of narrowband signals and therefore significantly limit the advantages of the aperture synthesis method. The narrow bandwidth of aperture synthesis radars is due to the limitation of the Van Cittert-Zernike theorem, in which the solution of integral equations involves the quasi-monochromatic approximation.

Another promising direction is the use of active-passive radar complexes [17-19]. Often, such complexes work in active and passive modes in different frequency bands [20].

It is possible to overcome the limitations of high-resolution imaging in the "blind zone" of radars due to the combination of active and passive radar methods and the use of ultra-wideband signals, taking into account the capabilities of the spectral aperture synthesis method [21]. Therefore, the problem of signal pro-

cessing algorithms developing for on-board systems with active aperture synthesis is extremely relevant.

Objectives. This work is devoted to the development of algorithms for incoherent and coherent radio imaging by RS with active aperture synthesis. It continues previous research [22, 23].

Initial data. Mathematical description of coherent and non-coherent images obtained by ultra-wideband radars

To obtain an algorithm for radar imaging from an aerospace carrier at angles close to the nadir, we use the geometry of the problem shown in Figure 1. At the mentioned angles, the classic RS have practically no range resolution. In this case, an underlying surface image in two Cartesian coordinates can be obtained by aperture synthesis methods implementing.

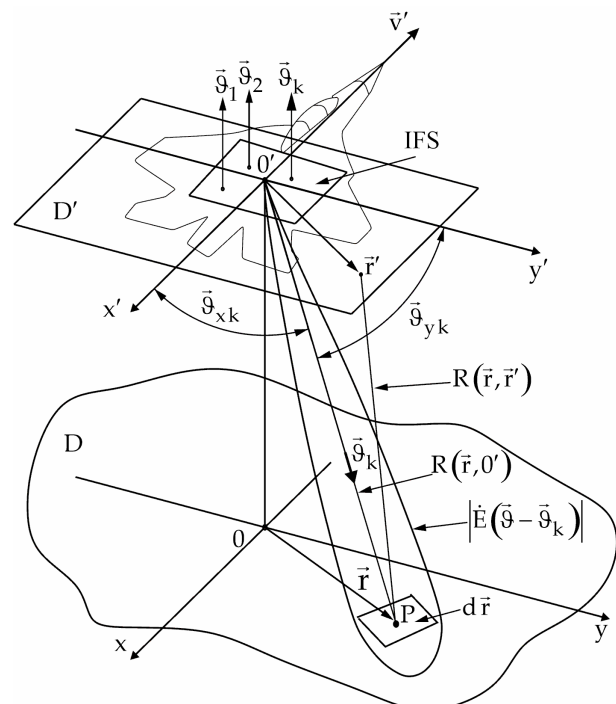


Fig. 1. Physical parameters and geometric relationships used while imaging algorithm obtaining

In Figure 1, the following designations are introduced: $x y$ is the underlying the surface coordinate system; $x' y'$ is the coordinate system associated with the phase center of the receiving antenna system; θ_{xk} is an angle between the x' -axes and the direction to the surface element $d\vec{r}$ centered at the point P ; θ_{yk} is an angle between the y' -axes and the direction to the surface element $d\vec{r}$ centered at the point P ; D' is a

flat receiving area; D is an irradiated underlying surface; \vec{r} is a radius vector directed to a reflecting point P on the underlying surface D ; \vec{r}' is a radius vector directed to the receiving point position in the receiving area D' ; $|\vec{E}(\vec{\vartheta} - \vartheta_k)|$ is a module of an antenna system Radiation Pattern (RP) focused in the direction ϑ_k ; $R(\vec{r}, 0')$ is the distance from the transmitting point $0'$ to the surface element $d\vec{r}$ centered at the point P ; $R(\vec{r}, \vec{r}')$ is the distance from a surface element $d\vec{r}$ centered at the point P to an receiving point in the receiving area D' ; IFS is Image Formation System.

IFS can be implemented using various imaging principles: a scanning system; a parallel-imaging system, in which the underlying surface is covered by several RP beams; a system that restores an image by coherence functions using, etc. The IFS outputs approximately correspond to the elements (pixels) of the obtained image of the observed surface elements $d\vec{r}$ with angular positions determined by the direction cosines $\vec{\vartheta}_1, \vec{\vartheta}_2, \dots, \vec{\vartheta}_k, \dots, \vec{\vartheta}_N$. In the case of a coherent image formation, the IFS output is proportional to the complex amplitudes of a received signals. When forming an incoherent image, power estimates are observed at the outputs.

To obtain the image formation algorithm, firstly we determine the probing signal model. It is advisable to represent a stochastic probing signal $s(t)$ in the spectral form as the inverse Fourier transform of its complex amplitude spectral density $\dot{S}(j2\pi f)$:

$$s(t) = \mathbb{F}_{f \rightarrow t}^{-1} \{ \dot{S}(j2\pi f) \}, \quad (1)$$

where $\mathbb{F}_{f \rightarrow t}^{-1} \{ \cdot \}$ is the inverse Fourier transform operator.

When probing the underlying surface, a signal reflected from the surface element $d\vec{r} = dx dy$ arrives to a receiving point \vec{r}' with the delay

$$t_z = \frac{R[\vec{r}(\vec{\vartheta}), \vec{r}']}{c} \approx \frac{2R[\vec{r}(\vec{\vartheta}), 0'] - \vec{\vartheta} \vec{r}'}{c}, \quad (2)$$

where $\vec{\vartheta} \vec{r}' = \vartheta_x x' + \vartheta_y y'$ is a scalar product of vectors $\vec{\vartheta}$ and \vec{r}' .

The summary field created by all surface elements in the receiving area $\vec{r}' \in D'$ approximately can be represented in the form

$$s(\vec{r}', t) = V_F^{-1} \{ \dot{S}\dot{F}(\vec{\vartheta}, f) \} = \int_{-\infty}^{\infty} \int_{-\infty}^{\infty} \dot{S}\dot{F}(\vec{\vartheta}, f) \exp \left\{ j2\pi f \left[t + c^{-1} \vec{\vartheta} \vec{r}' \right] \right\} df d\vec{\vartheta}, \quad (3)$$

where $V_F^{-1} \{ \cdot \}$ is the inverse V_F - transform operator [22, 24]; $\dot{S}\dot{F}(\vec{\vartheta}, f) = \dot{S}(j2\pi f) \dot{F}(\vec{\vartheta}, f)$ is a complex spectral image function which we consider as a coherent image; $\dot{F}(\vec{\vartheta}, f)$ is a specific (referred to the volume $dfd\vec{\vartheta}$) surface element $d\vec{r} = dx dy$ scattering coefficient, the area of which is recalculated to the solid angle $d\vec{\vartheta} = d\vartheta_x d\vartheta_y$.

The coefficient $\dot{F}(\vec{\vartheta}, f)$, as a complex function of the angular coordinates, represents the surface true coherent image at a certain frequency f . But in practice, the phase information contained in it is difficult to take into account. Therefore, in equation (3), the complex factor containing difficult-to-determine phase shifts at distances $2R[\vec{r}(\vec{\vartheta}), 0']$, will be added to the coefficient $\dot{F}(\vec{\vartheta}, f)$.

In terms of frequency f , the spectral function $\dot{S}\dot{F}(\vec{\vartheta}, f)$ is two-sided, that is, it is defined in the range $f \in (-\infty, \infty)$. In terms of variable $\vec{\vartheta}$, $\dot{S}\dot{F}(\vec{\vartheta}, f)$ is defined in the circle $\vec{\vartheta}_x^2 + \vec{\vartheta}_y^2 \leq 1$. Formally, the limits of integration over a variable $\vec{\vartheta}$ in further calculations will be extended to $\pm\infty$.

Since the V_F -transform is reversible, a coherent image $\dot{S}\dot{F}(\vec{\vartheta}, f)$ can be represented in the form

$$f^{-2} c^2 \dot{S}\dot{F}(\vec{\vartheta}, f) = V_F \{ s(\vec{r}', t) \} = \int_{-\infty}^{+\infty} \int_{-\infty}^{+\infty} s(\vec{r}', t) \exp \left\{ -j2\pi f \left(t + c^{-1} \vec{\vartheta} \vec{r}' \right) \right\} dt d\vec{r}', \quad (4)$$

where $V_F \{ \cdot \}$ is the direct V_F -transform operator.

For a complex analytical signal

$$\dot{s}(\vec{r}', t) = s(\vec{r}', t) + j s_{\perp}(\vec{r}', t)$$

a pair of transforms is valid

$$\dot{s}(\bar{r}', t) = \int_0^{+\infty} \int_{-\infty}^{+\infty} 2\dot{S}\dot{F}(\bar{\vartheta}, f) \times \exp\{j2\pi f[t + c^{-1}\bar{\vartheta}\bar{r}']\} d\bar{\vartheta} df = V_F^{-1} [2\dot{S}\dot{F}(\bar{\vartheta}, f)], \quad (5)$$

$$f^{-2}c^2 2\dot{S}\dot{F}(\bar{\vartheta}, f) = V_F [\dot{s}(\bar{r}', t)] = \int_{-\infty}^{+\infty} \int_{-\infty}^{+\infty} \dot{s}(\bar{r}', t) \exp\{-j2\pi f(t + c^{-1}\bar{\vartheta}\bar{r}')\} dt d\bar{r}', \quad (6)$$

where $s_{\perp}(\bar{r}', t)$ is a process associated with $s(\bar{r}', t)$ by Hilbert transforms over variable t . The spectral function $\dot{S}\dot{F}(\bar{\vartheta}, f)$ is equal to 0 while $f < 0$, and is doubled in positive frequencies range.

An important feature of the V_F -transforms use is their applicability for the description and analysis of ultra-wideband space-time fields and systems. For narrow-band fields, if the Quasi-Monochromatic Approximation (QMA) condition is satisfied, we can perform the transition $fc^{-1}\bar{\vartheta}\bar{r}' \approx f_0c^{-1}\bar{\vartheta}\bar{r}'$, where f_0 is the central frequency in the spectrum of a narrow-band signal [25]. In this case, equations (5) and (6) are converted into classical 3-dimensional Fourier transforms widely used in remote sensing, passive radar, and radio astronomy [26, 27].

We assume that the signals reflected from the underlying surface are random due to the random structure of surface's irregularities and probing signal stochasticity. Then the spectral components of the probing signal are uncorrelated with each other:

$$\langle \dot{S}(\bar{f}_1) \dot{S}^*(\bar{f}_2) \rangle = G(\bar{f}_1) \delta(\bar{f}_1 - \bar{f}_2), \quad (7)$$

where $G(\bar{f})$ is an emitted signal energy spectrum; $\langle \cdot \rangle$ is a statistical averaging sign.

Let us considered that reflections from various elements of an unregular surface (grass, shrubs, etc.), whose irregularities exceed the wavelength, are practically independent of each other. Then the values of the scattering coefficient at different angles are independent:

$$\langle [\dot{F}(\bar{\vartheta}_1, f) \dot{F}^*(\bar{\vartheta}_2, f)] \rangle = \sigma^0(\bar{\vartheta}_1, f) \delta(\bar{\vartheta}_1 - \bar{\vartheta}_2), \quad (8)$$

where $\sigma^0(\bar{\vartheta}_1, f)$ is Radar Cross-Section (RCS). This value is close to the surface scattering coefficient in terms of power. Therefore, in the problem being solved, we assume that it is a true incoherent surface image.

Then the correlation function of the signal $s(\bar{r}', t)$ in the receiving area can be represented the following

form:

$$R(\Delta\bar{r}', \tau) = \langle [s(\bar{r}'_1, t_1) s(\bar{r}'_2, t_2)] \rangle = V_F^{-1} [G\sigma^0(\bar{\vartheta}, f)] = \int_{-\infty}^{\infty} \int_{-\infty}^{\infty} G\sigma^0(\bar{\vartheta}, f) \exp\{j2\pi f(\tau + c^{-1}\bar{\vartheta}\Delta\bar{r}')\} df d\bar{\vartheta}, \quad (9)$$

where $\Delta\bar{r}' = \bar{r}'_1 - \bar{r}'_2$; $\tau = t_1 - t_2$; $G\sigma^0(\bar{\vartheta}, f)$ is an energy spectral function of the image, which, up to a factor $G(\bar{f})$, coincides with the true incoherent image $\sigma^0(\bar{\vartheta}, f)$ of the surface.

Equation (9) is reversible and the function $G\sigma^0(\bar{\vartheta}, f)$ is a direct V_F -transformation of the signal $s(\bar{r}', t)$ correlation function:

$$f^{-2}c^2 G\sigma^0(\bar{\vartheta}_1, f_1) = V_F [R(\Delta\bar{r}', \tau)] = \int_{-\infty}^{\infty} \int_{-\infty}^{\infty} R(\Delta\bar{r}', \tau) \times \exp\{-j2\pi f(\tau + c^{-1}\bar{\vartheta}\Delta\bar{r}')\} d\tau d\Delta\bar{r}'. \quad (10)$$

Similar relations hold for complex-conjugate analytical stationary homogeneous processes $\dot{s}(\bar{r}'_1, t_1)$ and $\dot{s}^*(\bar{r}'_2, t_2)$:

$$\dot{\Gamma}(\Delta\bar{r}', \tau) = \langle [\dot{s}(\bar{r}'_1, t_1) \dot{s}^*(\bar{r}'_2, t_2)] \rangle = V_F^{-1} [4G\sigma^0(\bar{\vartheta}, f)], \quad f^{-2}c^2 [4G\sigma^0(\bar{\vartheta}, f)] = V_F [\dot{\Gamma}(\Delta\bar{r}', \tau)], \quad (11)$$

where $\dot{\Gamma}(\Delta\bar{r}', \tau)$ is a cross-correlation function of processes $\dot{s}(\bar{r}'_1, t_1)$ and $\dot{s}^*(\bar{r}'_2, t_2)$. The spectral function $G\sigma^0(\bar{\vartheta}, f)$ in equation (11) is one-sided and is equal to zero while $f < 0$.

The obtained equations generalize the van Cittert-Zernike theorem in the analysis of wideband and ultrawideband signals in the far Fraunhofer zone. This theorem is widely used in passive RS and radio astronomy when the QMA condition is satisfied.

Let us rewrite the equation (9) in the following form

$$R(\tau, \Delta\bar{r}') = V_F^{-1} [G\sigma^0(\bar{\vartheta}, f)] = \int_{-\infty(F)}^{\infty} \dot{\Gamma}_{\sigma}(f, \Delta\bar{r}') \exp(j2\pi f \tau) df. \quad (12)$$

Here, the function is $\dot{\Gamma}_\sigma(f, \Delta\vec{r}')$ the Spectral Density of the Complex Spatial Coherence Function (SDCSCF) at the frequency f . It can be represented by the equation

$$\begin{aligned}\dot{\Gamma}_\sigma(f, \Delta\vec{r}') &= \mathbb{F}_{\vec{\vartheta} \rightarrow \Delta\vec{r}'}^{-1} \left[G\sigma^0(\vec{\vartheta}, f) \right] = \\ &= \mathbb{F}_{\tau \rightarrow f} \left[R(\tau, \Delta\vec{r}') \right].\end{aligned}\quad (13)$$

Equation (13) is the inverse spatial Fourier transform of the real spectral function of the image $G\sigma^0(\vec{\vartheta}, f)$, therefore it is its spatial spectrum

$$\begin{aligned}\dot{\Gamma}_\sigma(f, \Delta\vec{r}') &= \mathbb{F}_{\vec{\vartheta} \rightarrow \Delta\vec{r}'}^{-1} \left[G\sigma^0(\vec{\vartheta}, f) \right] = \\ &= \int_{-\infty(\Theta)}^{\infty} G\sigma^0(\vec{\vartheta}, f) \exp\left(j2\pi f \frac{\vec{\vartheta} \Delta\vec{r}'}{c} \right) d\vec{\vartheta}.\end{aligned}$$

The image spectral function can be restored by the direct spatial Fourier transform of the SDCSCF:

$$\begin{aligned}\frac{c^2}{f^2} G\sigma^0(\vec{\vartheta}, f) &= \mathbb{F}_{\Delta\vec{r}' \rightarrow \vec{\vartheta}} \left[\dot{\Gamma}_\sigma(f, \Delta\vec{r}') \right] = \\ &= \int_{-\infty(D')}^{\infty} \dot{\Gamma}_\sigma(f, \Delta\vec{r}') \exp\left(-j2\pi f \frac{\vec{\vartheta} \Delta\vec{r}'}{c} \right) \Delta\vec{r}'.\end{aligned}\quad (14)$$

The SDCSCF can also be found by the direct Fourier transform of the autocorrelation function $R(\tau, \Delta\vec{r}')$ in the time domain:

$$\dot{\Gamma}_\sigma(f, \Delta\vec{r}') = \mathbb{F}_{\tau \rightarrow f} \left[R(\tau, \Delta\vec{r}') \right].\quad (15)$$

Imaging algorithms based on the data of UWB stochastic signals processing

The above equations associate the signal fields and their spectral-correlation statistical characteristics on the scattering surface D and receiving area D' without specifying the processing operations. Thus, for the practical surface imaging, an explicit or implicit focusing of the IFS on its individual elements is necessary. Imaging is carried out either by scanning in a given sector of angles (sequential imaging), or by covering the sector with many RP beams (parallel imaging), or by implicit focusing methods associated with the use of complex coherence functions of observed radio fields. With explicit focusing on each direction, signal delays are introduced into the Amplitude-Phase Distribution (APD)

of the receiving antenna sensitivity corresponding to the time of arrival of oblique wave fronts from these directions. These delays correspond to the arrival time of wave fronts from these directions. Then, the delayed signals are summed. The phase delay operations of the signal spectral components and their subsequent in-phase integration (summation) are equivalent. All these operations are implemented by diagram-forming circuits (DFC), which are part of the IFS.

Initially, we consider an idealized continual APD of an antenna system, focused on the direction $\vec{\vartheta}_k$ and allowing phase control at each point of the receiving area $\vec{r}' \in D'$:

$$\dot{I}(f, \vec{r}', \vec{\vartheta}_k) = \dot{I}_0(f, \vec{r}') \exp\left(-j2\pi f \frac{\vec{\vartheta}_k \vec{r}'}{c} \right),\quad (16)$$

where $\dot{I}_0(f, \vec{r}')$ is the idealized APD that allows control of the amplitudes and phases of the received signals at each of its points. In the simplest case, an idealized APD can be described by the following equation:

$$\dot{I}_0(f, \vec{r}') = \begin{cases} 1, & \vec{r}' \in D'; \\ 0, & \vec{r}' \notin D'. \end{cases}\quad (17)$$

It is necessary to take into account that the RP $\dot{E}(f, \vec{\vartheta} - \vec{\vartheta}_k)$ and APD are connected by spatial Fourier transforms:

$$\begin{aligned}\dot{E}(f, \vec{\vartheta} - \vec{\vartheta}_k) &= \mathbb{F}_{\vec{r}' \rightarrow \vec{\vartheta}}^{-1} \left[\dot{I}(f, \vec{r}', \vec{\vartheta}_k) \right] = \\ &= \int_{-\infty(D')}^{\infty} \dot{I}(f, \vec{r}', \vec{\vartheta}_k) \exp\left[j2\pi f \vec{\vartheta} \frac{\vec{r}'}{c} \right] d\vec{r}',\end{aligned}\quad (18)$$

$$\begin{aligned}\dot{I}(f, \vec{r}', \vec{\vartheta}_k) &= \left(\frac{f}{c} \right)^2 \mathbb{F}_{\vec{\vartheta} \rightarrow \vec{r}'} \left[\dot{E}(f, \vec{\vartheta} - \vec{\vartheta}_k) \right] = \\ &= \int_{-\infty(D')}^{\infty} \dot{E}(f, \vec{\vartheta} - \vec{\vartheta}_k) \exp\left(-j2\pi f \frac{\vec{\vartheta} \vec{r}'}{c} \right) d\vec{r}'.\end{aligned}\quad (19)$$

Then, in the case of IFS focusing on the direction $\vec{\vartheta}_k$, the received signal can be represented as follows:

$$\begin{aligned}s(t, \vec{\vartheta}_k) &= \int_{-\infty(\Theta)}^{\infty} \int_{-\infty(F)}^{\infty} \int_{-\infty(D')}^{\infty} \dot{K}(j2\pi f) \dot{I}(f, \vec{r}', \vec{\vartheta}_k) \dot{S}\dot{F}(\vec{\vartheta}, f) \times \\ &\times \exp\left\{ j2\pi f \left(t + \frac{\vec{\vartheta} \vec{r}'}{c} \right) \right\} d\vec{r}' df d\vec{\vartheta} = \int_{-\infty(F)}^{\infty} \int_{-\infty(\Theta)}^{\infty} \dot{K}(j2\pi f) \times \\ &\times \dot{F}(f, \vec{\vartheta} - \vec{\vartheta}_k) \dot{S}\dot{F}(\vec{\vartheta}, f) \exp\{j2\pi f t\} df d\vec{\vartheta},\end{aligned}\quad (20)$$

where $\dot{K}(j2\pi f)$ is a transmission ratio of IFS. For antenna arrays, these are the transmission coefficients of antenna-feeder paths and receiving devices connected to the outputs of individual elementary antennas that are part of the array.

Taking into account equations (7) and (8), we find the average power of the received signal, which is an estimate of the integral incoherent image

$$\begin{aligned} \hat{P}(\bar{\vartheta}_k) &= \left\langle s^2(t, \bar{\vartheta}_k) \right\rangle = \int_{-\infty(F)}^{\infty} |\dot{K}(j2\pi f)|^2 \times \\ &\times \int_{-\infty(\Theta)}^{\infty} \left| \dot{E}(f, \bar{\vartheta} - \bar{\vartheta}_k) \right|^2 G\sigma^0(\bar{\vartheta}, f) d\bar{\vartheta} df, \quad (21) \end{aligned}$$

where $(\hat{\cdot})$ is estimation sign.

Image estimation at each frequency is the result of smoothing (defocusing) of the true image $G\sigma^0(\bar{\vartheta}, f)$ by RP $\left| \dot{E}(f, \bar{\vartheta} - \bar{\vartheta}_k) \right|^2$ in terms of power:

$$G\hat{\sigma}^0(\bar{\vartheta}_k, f) = \int_{-\infty(\Theta)}^{\infty} \left| \dot{E}(f, \bar{\vartheta} - \bar{\vartheta}_k) \right|^2 G\sigma^0(\bar{\vartheta}, f) d\bar{\vartheta}. \quad (22)$$

Applying the spatial Fourier transforms to the integrands $\left| \dot{E}(f, \bar{\vartheta} - \bar{\vartheta}_k) \right|^2$ and $G\sigma^0(\bar{\vartheta}, f)$, we obtain

$$\begin{aligned} G\hat{\sigma}^0(\bar{\vartheta}_k, f) &= \\ &= \int_{-\infty(\Delta\bar{r}', D')}^{\infty} \dot{R}_{APD}(f, \Delta\bar{r}', \bar{\vartheta}_k) \dot{\Gamma}_{\sigma}(f, \Delta\bar{r}') d\Delta\bar{r}', \quad (23) \end{aligned}$$

where $\dot{R}_{ADP}(f, \Delta\bar{r}', \bar{\vartheta}_k)$ is an Autocorrelation Function of APD (AF APD), which has the following form

$$\begin{aligned} \dot{R}_{APD}(f, \Delta\bar{r}', \bar{\vartheta}_k) &= \\ &= \int_{-\infty(D')}^{\infty} \dot{I}(f, \bar{r}', \bar{\vartheta}_k) \dot{I}^*(f, \bar{r}' - \Delta\bar{r}', \bar{\vartheta}_k) d\bar{r}'. \quad (24) \end{aligned}$$

For the APD (16), the AF APD is described by the equation

$$\begin{aligned} \dot{R}_{APD}(f, \Delta\bar{r}', \bar{\vartheta}_k) &= \\ &= \dot{R}_{0(APD)}(f, \Delta\bar{r}') \exp\left(-j2\pi f \frac{\bar{\vartheta}_k \Delta\bar{r}'}{c}\right), \quad (25) \end{aligned}$$

where

$$\begin{aligned} \dot{R}_{0(APD)}(f, \Delta\bar{r}') &= \\ &= \int_{-\infty(D')}^{\infty} \dot{I}_0(f, \bar{r}') \dot{I}_0^*(f, \bar{r}' - \Delta\bar{r}') d\bar{r}' \quad (26) \end{aligned}$$

is the APD autocorrelation function of the initial, unfocused antenna system.

Considering (25), image estimation (23) can be represented in the following form

$$\begin{aligned} G\hat{\sigma}^0(\bar{\vartheta}_k, f) &= \int_{-\infty(\Delta\bar{r}', D')}^{\infty} \dot{R}_{0(APD)}(f, \Delta\bar{r}') \times \\ &\times \dot{\Gamma}_{\sigma}(f, \Delta\bar{r}') \exp\left(-j2\pi f \frac{\bar{\vartheta}_k \Delta\bar{r}'}{c}\right) d\Delta\bar{r}', \quad (27) \end{aligned}$$

where $G\hat{\sigma}^0(\bar{\vartheta}_k, f)$ is calculated as the Fourier transform of the product of the SDCSCF (13) and the AF APD (26).

The SDCSCF $\dot{\Gamma}_{\sigma}(f, \Delta\bar{r}')$ should be considered as the spatial image spectrum, while the AF APD $\dot{R}_{0(APD)}(f, \Delta\bar{r}')$ is the spatial transmission ratio of these spectral components. Then the integral image (21) has a form:

$$\begin{aligned} \hat{P}(\bar{\vartheta}_k) &= \int_{-\infty(F)}^{\infty} |\dot{K}(j2\pi f)|^2 \int_{-\infty(\Delta\bar{r}', D')}^{\infty} \dot{R}_{0(APD)}(f, \Delta\bar{r}') \times \\ &\times \dot{\Gamma}_{\sigma}(f, \Delta\bar{r}') \exp\left(-j2\pi f \frac{\bar{\vartheta}_k \Delta\bar{r}'}{c}\right) d\Delta\bar{r}' df. \quad (28) \end{aligned}$$

In equation (28), focusing on the direction $\bar{\vartheta}_k$ is ensured by the exponential factor and by the integration over the variable $\Delta\bar{r}'$.

The signals can be filtered into narrow-band components in the frequency bands with frequency response $|\dot{K}_m(j2\pi f)|$, so that the integrands in the internal integrals (21) and (28) are independent of the frequency and satisfy the QMA conditions. Then the integration operations in equation (28) can be replaced by summation:

$$\begin{aligned} \hat{P}(\bar{\vartheta}_k) &= 2 \sum_{m=1}^M \Delta F_m \int_{-\infty(\Theta)}^{\infty} \left| \dot{F}(f_{0m}, \bar{\vartheta} - \bar{\vartheta}_k) \right|^2 \times \\ &\quad \times G \sigma^0(\bar{\vartheta}, f_{0m}) d\bar{\vartheta} = 2 \sum_{m=1}^M \Delta F_m \times \\ &\quad \times \int_{-\infty(\Delta \bar{r}', D')}^{\infty} \dot{R}_{0(\text{APD})}(f_{0m}, \Delta \bar{r}') \dot{I}_\sigma(f_{0m}, \Delta \bar{r}') \times \\ &\quad \times \exp\left(-j2\pi f_{0m} \frac{\bar{\vartheta}_k \Delta \bar{r}'}{c}\right) d\Delta \bar{r}', \end{aligned} \quad (29)$$

where

$$\begin{aligned} 2\Delta F_m &= \int_{-\infty}^{\infty} \left| \dot{K}_m(j2\pi f) \right|^2 df, \quad (30) \\ \left| \dot{K}_m(j2\pi f) \right|^2 &= \left| \dot{K}_m[-j2\pi(f + f_{0m})] \right|^2 + \\ &+ \left| \dot{K}_m[j2\pi(f - f_{0m})] \right|^2 \approx \left| \dot{K}_m[-j2\pi(f + f_{0m})] \right|^2 + \\ &+ \left| \dot{K}_m[j2\pi(f - f_{0m})] \right|^2. \end{aligned} \quad (31)$$

The obtained equations indicate the possible operations that can be performed on the received signals to form an underlying surface image. In this article, we consider two methods for incoherent imaging. The explicit focusing method has been considered in formulas (20) and (21). To implement it, it is necessary to cover a given observation sector with a set of RP beams and estimate the signal power for each beam direction. Generally, focusing on operations can be conducted by performing delays of the ultrawideband signal corresponding to the delays of the incident wave front. This can also be done after filtering the signal into separate processes, using appropriate phase delays and summation. Images obtained at different frequencies must be integrated (summed).

The second imaging variant is based on the use of equation (28) or (29) and uses the concepts of coherence functions and AF APD. Equation (29) assumes the filtering of an ultra-wideband complex analytical signal into narrow frequency bands with transfer coefficients $\dot{K}_m(j2\pi f) = \dot{K}_m[j2\pi(f - f_{0m})]$ (it satisfies the QMA condition), integration, and summation of images. The analytical signal has a one-sided spectrum and allows to obtain the coherence function only at positive frequencies that have a physical realization. Otherwise, it is necessary to introduce into the processing algorithm (29) the second frequency $-f_{0m}$, which has no physical realization. Technically, an analytical signal can be

formed, for example, using quadrature detectors [28, 29].

Processing of signals received by an idealized continuum aperture

The narrow-band analytical signal in the m -th frequency band for each point $\bar{r}' \in D'$ of the aperture (17) can be represented as follows:

$$\begin{aligned} \dot{s}_m(t, \bar{r}') &= \dot{S}_m(t, \bar{r}') \exp(j2\pi f_{0m} t) \approx \int_{-\infty}^{\infty} \int_{-\infty}^{\infty} 2\dot{S}\dot{F}(\bar{\vartheta}, f) \times \\ &\times \dot{I}_0(\bar{r}', f_{0m}) \dot{K}_m(j2\pi f) \exp\left\{j2\pi \left[ft + f_{0m} c^{-1} \bar{\vartheta} \bar{r}'\right]\right\} df d\bar{\vartheta} = \\ &= \exp(j2\pi f_{0m} t) \dot{I}_0(\bar{r}', f_{0m}) \int_{-\infty}^{\infty} \dot{S}_m(\bar{\vartheta}, t) \times \\ &\quad \times \exp\left\{j2\pi f_{0m} \left(c^{-1} \bar{\vartheta} \bar{r}'\right)\right\} d\bar{\vartheta}. \end{aligned} \quad (32)$$

In equation (32)

$$\begin{aligned} \dot{S}_m(t, \bar{r}') &= \dot{I}_0(\bar{r}', f_{0m}) \int_{-\infty}^{\infty} \dot{S}_m(\bar{\vartheta}, t) \times \\ &\quad \times \exp\left\{j2\pi f_{0m} \left(c^{-1} \bar{\vartheta} \bar{r}'\right)\right\} d\bar{\vartheta} \end{aligned} \quad (33)$$

is a complex envelope of the signal received and filtered at a point $\bar{r}' \in D'$ by a narrow band filter with a frequency response $\dot{K}_m(j2\pi f)$. To simplify the formulas, the indices corresponding to the numbers of frequency bands after signals filtering will not be indicated further in the article, where this is not of fundamental importance.

So that in further transformations the frequencies $f_0 = f_{0m}$ are only in the positive frequency range, we use analytical signals with a one-sided spectrum. Let us find the complex coherence function of the analytical signal in the m -th frequency band:

$$\begin{aligned} \dot{I}(\tau, \Delta \bar{r}') &= \left\langle \dot{s}(t, \bar{r}') \dot{s}^*(t - \tau, \bar{r}' - \Delta \bar{r}') \right\rangle = \\ &= \left\langle \dot{S}(t, \bar{r}') \dot{S}^*(t - \tau, \bar{r}' - \Delta \bar{r}') \right\rangle \exp(j2\pi f_0 \tau) = \exp(j2\pi f_0 \tau) \times \\ &\quad \times \dot{I}_0(\bar{r}', f_0) \dot{I}_0^*(\bar{r}' - \Delta \bar{r}', f_0) \times \int_{-\infty}^{\infty} \left\langle \dot{S}(\bar{\vartheta}_1, t) \times \right. \\ &\quad \times \dot{S}^*(\bar{\vartheta}_2, t - \tau) \left. \right\rangle \exp\left\{j2\pi f_0 \left(c^{-1} \bar{\vartheta}_1 \bar{r}' - \right. \right. \\ &\quad \left. \left. - j2\pi f_0 \left(c^{-1} \bar{\vartheta}_2 (\bar{r}' - \Delta \bar{r}')\right)\right\} d\bar{\vartheta}_1 d\bar{\vartheta}_2. \end{aligned} \quad (34)$$

For $\tau = 0$, the spatial coherence function has the following form:

$$\begin{aligned} \dot{\Gamma}(0, \Delta\vec{r}') &= \left\langle \dot{s}(t, \vec{r}') \dot{s}^*(t, \vec{r}' - \Delta\vec{r}') \right\rangle = \left\langle \dot{S}(t, \vec{r}') \times \right. \\ &\times \dot{S}^*(t, \vec{r}' - \Delta\vec{r}') \left. \right\rangle = 4\Delta F \dot{I}_0(\vec{r}', f_0) \dot{I}_0^*(\vec{r}' - \Delta\vec{r}', f_0) \times \\ &\times \int_{-\infty}^{\infty} G\sigma^0(\bar{\vartheta}, f) \exp\left\{j2\pi f_0 \left(c^{-1}\bar{\vartheta}\Delta\vec{r}'\right)\right\} d\bar{\vartheta}. \quad (35) \end{aligned}$$

Additionally, we take into account (7) and (8) in equation (36), then

$$\begin{aligned} \left\langle \dot{S}(\bar{\vartheta}_1, t) S^*(\bar{\vartheta}_2, t) \right\rangle &= \int_{-\infty}^{\infty} \int_{-\infty}^{\infty} 4 \left\langle \dot{S}\dot{F}(\bar{\vartheta}_1, f_1) \times \right. \\ &\times \dot{S}^*\dot{F}^*(\bar{\vartheta}_2, f_2) \left. \right\rangle \dot{K}(j2\pi f_1) \dot{K}^*(j2\pi f_2) \times \\ &\times \exp\{j2\pi(f_1 - f_2)t\} df_1 df_2 = \\ &= \delta(\bar{\vartheta}_1 - \bar{\vartheta}_2) \int_{-\infty}^{\infty} 4G\sigma^0(\bar{\vartheta}_1, f) \left| \dot{K}(j2\pi f) \right|^2 df. \quad (36) \end{aligned}$$

For a narrow m -th frequency response band $\left| \dot{K}(j2\pi f) \right| = \left| \dot{K}[j2\pi(f - f_0)] \right|$ in the vicinity of the frequency f_0 , the following equation can be applied:

$$\begin{aligned} \int_{-\infty}^{\infty} 4G\sigma^0(\bar{\vartheta}, f_0) \left| \dot{K}[j2\pi(f - f_0)] \right|^2 df &\approx \\ &\approx 4G\sigma^0(\bar{\vartheta}, f_0) \Delta F. \quad (37) \end{aligned}$$

Here, it is considered that the analytical signal has a one-sided spectrum, doubled in amplitude.

To obtain a practical image formation algorithm, it is necessary to correctly substantiate the signal averaging procedure, indicated by the sign $\langle \cdot \rangle$. When calculating the coherence function, this mathematical operation is represented by the following expression:

$$\begin{aligned} \dot{\Gamma}(\tau, \Delta\vec{r}') &= \left\langle \dot{S}(t, \vec{r}') \dot{S}^*(t - \tau, \vec{r}' - \Delta\vec{r}') \right\rangle = \left\langle \dot{S}_1 \dot{S}_2^* \right\rangle = \\ &= \int_{-\infty}^{\infty} \int_{-\infty}^{\infty} \dot{S}_1 \dot{S}_2^* p(\dot{S}_1 \dot{S}_2^*) d\dot{S}_1 d\dot{S}_2^*, \quad (38) \end{aligned}$$

where $p(\dot{S}_1 \dot{S}_2^*)$ is the joint probability density functional of the processes $\dot{S}(t, \vec{r}')$ and $\dot{S}^*(t - \tau, \vec{r}' - \Delta\vec{r}')$.

Algorithmically, this formula has no physical implementation. However, in practical cases, the necessary averaging procedure can be performed based on the mean value theorem. For $T \rightarrow \infty$ and $D' \rightarrow \infty$, it is strictly justified for determining the statistical characteristics of ergodic processes:

$$\begin{aligned} \dot{\Gamma}_{TD'}(\tau, \Delta\vec{r}') &= \\ &= \frac{1}{TD'} \int_{D'} \int_0^T \dot{S}(t, \vec{r}') \dot{S}^*(t - \tau, \vec{r}' - \Delta\vec{r}') dt d\vec{r}', \quad (39) \end{aligned}$$

where D' is observation area.

In contrast to equation (39) for the mathematical expectation of the signal's product, formula (40) for their average value is physically realizable in the form of an algorithm for the received field processing. Note that many optimization problems in which the average initial data values are given by the probabilistic equation (39) lead to physically realizable solutions in the form (40) [24].

An approximate average of the product of these functions can be obtained by integrating them over time only:

$$\Gamma_{\sigma}(\tau, \Delta\vec{r}') = \frac{1}{T} \int_0^T \dot{S}(t, \vec{r}') \dot{S}^*(t - \tau, \vec{r}' - \Delta\vec{r}') dt d\vec{r}'. \quad (40)$$

Additionally, averaging equation (41) over spatial coordinates and considering the approximate equalities of mathematical expectations and average values, we obtain:

$$\begin{aligned} \dot{\Gamma}_{TD'}(0, \Delta\vec{r}') &\approx \frac{1}{D'} \int_{D'} \left\langle \dot{S}(t, \vec{r}') \dot{S}^*(t, \vec{r}' - \Delta\vec{r}') \right\rangle d\vec{r}' \frac{4\Delta F}{D'} \times \\ &\times \int_{D'} \dot{I}_0(\vec{r}', f_0) \dot{I}_0^*(\vec{r}' - \Delta\vec{r}', f_0) d\vec{r}' \int_{-\infty}^{\infty} G\sigma^0(\bar{\vartheta}, f_0) \times \\ &\times \exp\left\{j2\pi f_0 \left(c^{-1}\bar{\vartheta}\Delta\vec{r}'\right)\right\} d\bar{\vartheta} = \\ &= \frac{4\Delta F}{D'} \dot{R}_{0(ADP)}(\Delta\vec{r}', f_0) \dot{\Gamma}_{\sigma}(\Delta\vec{r}', f_0). \quad (41) \end{aligned}$$

Comparing this result with equations (22) and (23), we conclude that the incoherent image estimation $G\sigma^0(\bar{\vartheta}_k, f_{0m})$ at each filtered frequency f_{0m} can be found as the Fourier-transform of the product $\dot{R}_{ADP}(\Delta\vec{r}', f_0) \dot{\Gamma}_{\sigma}(f_0, \Delta\vec{r}')$:

$$\begin{aligned} & \mathbb{F}_{\Delta\vec{r}' \rightarrow \vec{\vartheta}} \left[\dot{\Gamma}_{TD'}(0, \Delta\vec{r}') \right] \approx \frac{4\Delta F}{D'} \times \\ & \times \int_{-\infty(\Delta\vec{r}', D')}^{\infty} \dot{R}_{0(ADP)}(f_0, \Delta\vec{r}') \dot{\Gamma}_{\sigma}(f_0, \Delta\vec{r}') \times \\ & \times \exp\left(-j2\pi f_0 \frac{\vec{\vartheta}_k \Delta\vec{r}'}{c}\right) d\Delta\vec{r}' = \frac{4\Delta F}{D'} G\hat{\sigma}^0(\vec{\vartheta}_k, f_0). \quad (42) \end{aligned}$$

It corresponds to the classical van Cittert–Zernike theorem. It should be note, that in a narrow frequency band in the vicinity of each frequency f_{0m} , the QMA condition is satisfied. In the obtained equation, it is necessary to use formulas (40) or (41) to form the spatial coherence functions $\dot{\Gamma}_{TD'}(0, \Delta\vec{r}')$ or $\dot{\Gamma}_{\sigma}(0, \Delta\vec{r}')$.

Thus, if there is an aperture with a given APD in the observation area D' , the spatial coherence function of the received field is multiplied by the AF APD. Then, to restore the image in accordance with the van Cittert–Zernike theorem, it is necessary to apply the spatial Fourier transform to equation (42). The Fourier transform of the integrand's product leads to the convolution of the true incoherent image $G\sigma^0(\vec{\vartheta}_k, f_0)$ and RP:

$$\begin{aligned} & \mathbb{F}_{\Delta\vec{r}' \rightarrow \vec{\vartheta}} \left[\dot{\Gamma}_{TD'}(0, \Delta\vec{r}') \right] = \frac{4\Delta F}{D'} G\hat{\sigma}^0(\vec{\vartheta}_k, f_0) = \\ & = \frac{4\Delta F}{D'} \int_{-\infty(\Theta)}^{\infty} \left| \dot{E}(f, \vec{\vartheta} - \vec{\vartheta}_k) \right|^2 G\sigma^0(\vec{\vartheta}_k, f_0) d\vec{\vartheta}. \quad (43) \end{aligned}$$

In the obtained equation, the function $\dot{\Gamma}_{\sigma}(f, \Delta\vec{r}')$ is the complex spatial spectrum of the real spectral function $G\sigma^0(\vec{\vartheta}_k, f_0)$, and the function $\dot{R}_{0(ADP)}(f, \Delta\vec{r}')$ is the spatial complex transmission coefficient of an antenna system. At the same time, the spatial configuration of the antenna system and its APD must ensure the registration of the maximum number of harmonics of the function $G\sigma^0(\vec{\vartheta}_k, f_0)$ spectrum. The function $\hat{\sigma}^0(\vec{\vartheta}_k, f_0)$ is a smoothed estimate of the true image $\sigma^0(\vec{\vartheta}_k, f_0)$ with loss of resolution by an amount determined by the type and width of the pattern $\left| \dot{E}(f, \vec{\vartheta} - \vec{\vartheta}_k) \right|^2$. Thus, to implement the second algorithm for incoherent imaging in the presence of an idealized continual APD, it is necessary to perform the following algorithmic operations on the received signal in the area of its registration.

1. It is necessary to filter the received ultra-wideband space-time signal into narrow frequency bands that satisfy the QMA condition.

2. We estimate the complex functions of spatial coherence $\dot{\Gamma}_{TD'}(0, \Delta\vec{r}')$ in each individual frequency band. It can be done by multiplying the complex amplitudes of the signals received by the antenna system elements at points \vec{r}' , and integrating the product over t and \vec{r}' :

$$\begin{aligned} & \dot{\Gamma}_{TD'}(0, \Delta\vec{r}') = \\ & = \frac{1}{TD'} \int_0^T \int_{D'} \dot{S}(t, \vec{r}') \dot{S}^*(t, \vec{r}' - \Delta\vec{r}') dt d\vec{r}'. \quad (44) \end{aligned}$$

3. In accordance with the Van Cittert–Zernike theorem, we calculate the image estimates $G\sigma^0(\vec{\vartheta}_k, f_0)$, applying the spatial Fourier transform to $\dot{\Gamma}_{TD'}(0, \Delta\vec{r}')$:

$$\begin{aligned} & \frac{4\Delta F}{D'} G\hat{\sigma}^0(\vec{\vartheta}_k, f_0) = \\ & = \int_{-\infty(\Delta\vec{r}', D')}^{\infty} \dot{\Gamma}_{TD'}(0, \Delta\vec{r}') \exp\left(-j2\pi f \frac{\vec{\vartheta}_k \Delta\vec{r}'}{c}\right) d\Delta\vec{r}'. \quad (45) \end{aligned}$$

This operation must be performed in each subband frequency of a wideband or ultra-wideband space-time signal.

4. Then it is necessary to sum the obtained results in accordance with formula (29):

$$\hat{P}(\vec{\vartheta}_k) = 4 \sum_{i=1}^N \Delta F_i G\hat{\sigma}_i^0(\vec{\vartheta}_k, f_0). \quad (46)$$

The resulting integral image will be more informative, because will contain the summary information contained in each frequency band. Obviously, each image formed in different frequency bands can be studied separately.

The proposed algorithm is applicable for an idealized antenna aperture (16) and (17) with the possibility of the phase changing at each point \vec{r}' of the receiving area. The implementation of such an aperture is possible in optics, however, in the radio wave range, its implementation is impossible. Therefore, it is advisable to obtain an appropriate signal processing algorithm for the case of real antennas, such as AR.

Practical imaging algorithm using antenna arrays

In real AR, the receiving area is discretely filled with apertures of elementary antennas with a basic APD

$$\dot{I}(f, \vec{r}') = \sum_{i=1}^N \dot{I}_{ai}(f, \vec{r}' - \vec{r}'_i). \quad (47)$$

Reception of signals and control of their delays are possible only at the outputs of elementary antennas with phase centers at points \vec{r}'_i . APD for an AA subjected to amplitude-phase control and focused on the direction $\vec{\Theta}_k$, has the following form

$$\dot{I}(f, \vec{r}', \vec{\Theta}_k) = \sum_{i=1}^N \dot{I}_{ai}(f, \vec{r}' - \vec{r}'_i) \exp\left[-j2\pi f \frac{\vec{\Theta}_k \vec{r}'_i}{c}\right]. \quad (48)$$

Its AF APD can be represented by the equation

$$\begin{aligned} \dot{R}_{ADP}(f, \Delta \vec{r}', \vec{\Theta}_k) &= \sum_{i=1}^N \sum_{j=1}^N \exp\left[-j2\pi f \frac{\vec{\Theta}_k (\vec{r}'_i - \vec{r}'_j)}{c}\right] \times \\ &\times \dot{R}_{0ij(ADP)}\left[f, \Delta \vec{r}' - (\vec{r}'_i - \vec{r}'_j)\right], \end{aligned} \quad (49)$$

where

$$\begin{aligned} \dot{R}_{0ij(ADP)}\left[f, \Delta \vec{r}' - (\vec{r}'_i - \vec{r}'_j)\right] &= \\ &= \int_{-\infty(D')}^{\infty} \dot{I}_{ai}(f, \vec{r}' - \vec{r}'_i) \dot{I}_{aj}(f, \vec{r}' - \Delta \vec{r}' - \vec{r}'_j) d\vec{r}' \end{aligned} \quad (50)$$

are cross-correlation functions of basic APDs $\dot{I}_{ai}(f, \vec{r}' - \vec{r}'_i)$ of AA elements.

We substitute equation (49) into (23) and obtain

$$\begin{aligned} G\hat{\sigma}^0(\vec{\Theta}_k, f) &= \\ &= \sum_{i=1}^N \sum_{j=1}^N \dot{I}_{ij}(f) \exp\left[-j2\pi f \frac{\vec{\Theta}_k (\vec{r}'_i - \vec{r}'_j)}{c}\right], \end{aligned} \quad (51)$$

where

$$\begin{aligned} \dot{I}_{ij}(f) &= \int_{-\infty(\Delta \vec{r}', D')}^{\infty} \dot{R}_{0ij(ADP)}\left[f, \Delta \vec{r}' - (\vec{r}'_i - \vec{r}'_j)\right] \times \\ &\times \dot{I}_{\sigma}(f, \Delta \vec{r}') d\Delta \vec{r}' = \int_{-\infty(\Theta)}^{\infty} \dot{E}_{ai}(f, \vec{\Theta}) \dot{E}_{aj}^*(f_0, \vec{\Theta}) \times \\ &\times G\hat{\sigma}^0(\vec{\Theta}_k, f) \exp\left[j2\pi f \vec{\Theta} \frac{(\vec{r}'_i - \vec{r}'_j)}{c}\right] d\vec{\Theta}. \end{aligned} \quad (52)$$

Equation (51) shows that the estimates of incoherent images $G\hat{\sigma}^0(\vec{\Theta}_k, f_{0m})$ are calculated by applying the discrete Fourier transform to the coefficients $\dot{I}_{ij}(f_{0m})$. These coefficients are the result of integrating the products of the complex function of spatial coherence and the cross-correlation functions of the basic APDs of AA elements. After filtering the signals over narrow frequency bands, as in the previous problem with an idealized aperture, it is necessary to substitute discrete frequency values $f = f_{0m}$ into the obtained equations (51) and (52).

It should be noted that the numbering of the antennas $i = \overline{1, N}$, $j = \overline{1, N}$, for simplicity, is chosen sequentially, regardless of whether the AA is one-dimensional or two-dimensional. The RP of all elementary antennas are the same and have the form of the Fourier transform of the corresponding APDs:

$$\begin{aligned} \dot{E}_{ai}(\vec{\Theta}, f, \vec{r}'_i) &= \int_{-\infty(D')}^{\infty} \dot{I}_{ai}(\vec{r}' - \vec{r}'_i, f) \times \\ &\times \exp\left\{j2\pi f \left(c^{-1} \vec{\Theta} \vec{r}'\right)\right\} d\vec{r}' = \left| \begin{matrix} \vec{r}' - \vec{r}'_i = \vec{r}'_i \\ \vec{r}' = \vec{r}'_i + \vec{r}'_i \end{matrix} \right| = \\ &= \exp\left\{j2\pi f \left(c^{-1} \vec{\Theta} \vec{r}'_i\right)\right\} \int_{-\infty(D')}^{\infty} \dot{I}_{ai}(\vec{r}'_i, f) \times \\ &\times \exp\left\{j2\pi f c^{-1} \vec{\Theta} \vec{r}'_i\right\} d\vec{r}'_i = \dot{E}_{ai}(\vec{\Theta}, f) \times \\ &\times \exp\left\{j2\pi f \left(c^{-1} \vec{\Theta} \vec{r}'_i\right)\right\}. \end{aligned} \quad (53)$$

The RPs of different AA elements differ only in phase multipliers $\exp\left\{j2\pi f \left(c^{-1} \vec{\Theta} \vec{r}'_i\right)\right\}$, characterizing the position of their phase centers \vec{r}'_i . These multipliers arise in a natural way when a wave is registered along its incidence front in the form of a delay or ahead in phase in relation to the origin of coordinates.

The summarized (integral) image can be represented as follows:

$$\hat{P}(\vec{\Theta}_k) = \sum_{m=1}^M 2\Delta F_m G\hat{\sigma}_m^0(\vec{\Theta}_k, f_{0m}). \quad (54)$$

The obtained equations describe the mathematical structure of the image and the physical meaning of some mathematical operations. However, the equations do not have information about what specific algorithmic operations must be performed on the received signal to form the image. To solve this problem, we assume that the

signals after filtering are received by each elementary antenna in separate narrow frequency bands and that the signals in each such band satisfy the QMA condition. Analytical complex signals with a one-sided spectrum at the output of the i -th antenna in each band have the form:

$$\begin{aligned} \dot{s}(t, \vec{r}_i') &= \dot{S}(t, \vec{r}_i') \exp(j2\pi f_0 t) = \int_{-\infty(D_i')}^{\infty} \int_{-\infty}^{\infty} \int_{-\infty}^{\infty} 2\dot{S}\dot{F}(\vec{\vartheta}, f) \times \\ &\times \dot{I}_{ai}(\vec{r}' - \vec{r}_i', f_0) \dot{K}[j2\pi(f - f_0)] \times \\ &\times \exp\left\{j2\pi\left[ft + f_0 c^{-1} \vec{\vartheta} \vec{r}'\right]\right\} df d\vec{\vartheta} d\vec{r}' = \exp(j2\pi f_0 t) \times \\ &\times \int_{-\infty}^{\infty} \dot{S}(\vec{\vartheta}, t) \dot{E}_{ai}(\vec{\vartheta}, f_0) \exp\left\{j2\pi f_0 \left(c^{-1} \vec{\vartheta} \vec{r}_i'\right)\right\} d\vec{\vartheta}, \quad (55) \end{aligned}$$

where

$$\begin{aligned} \dot{S}(\vec{\vartheta}, t) \exp(j2\pi f_0 t) &= \int_{-\infty}^{\infty} 2\dot{S}\dot{F}(\vec{\vartheta}, f) \times \\ &\times \dot{K}[j2\pi(f - f_0)] \exp\{j2\pi(ft)\} df, \quad (56) \end{aligned}$$

$$\begin{aligned} \dot{S}(t, \vec{r}_i') &= \int_{-\infty}^{\infty} \dot{S}(\vec{\vartheta}, t) \dot{E}_{ai}(\vec{\vartheta}, f_0) \times \\ &\times \exp\left\{j2\pi f_0 \left(c^{-1} \vec{\vartheta} \vec{r}_i'\right)\right\} d\vec{\vartheta}, \quad (57) \end{aligned}$$

and $\dot{E}_{ai}(\vec{\vartheta}, f_0)$ is described by equation (53).

Consider the complex spatial function of mutual coherence of complex analytical signals, the real and imaginary parts of which are formed at the outputs of two arbitrary i -th and j -th elementary antennas:

$$\begin{aligned} \left\langle \dot{S}(t, \vec{r}_i') \dot{S}^*(t, \vec{r}_j') \right\rangle &= \int_{-\infty}^{\infty} \int_{-\infty}^{\infty} \left\langle \dot{S}(\vec{\vartheta}_1, t) \dot{S}_2^*(\vec{\vartheta}_2, t) \right\rangle \times \\ &\times \dot{E}_{ai}(\vec{\vartheta}_1, f_0) \dot{E}_{aj}^*(\vec{\vartheta}_2, f_0) \times \\ &\times \exp\left\{j2\pi f_0 c^{-1} \left(\vec{\vartheta}_1 \vec{r}_i' - \vec{\vartheta}_2 \vec{r}_j'\right)\right\} d\vec{\vartheta}_1 d\vec{\vartheta}_2 = \int_{-\infty}^{\infty} 4\Delta F \times \\ &\times G\sigma^0(\vec{\vartheta}, f_0) \dot{E}_{ai}(\vec{\vartheta}, f_0) \dot{E}_{aj}^*(\vec{\vartheta}, f_0) \times \\ &\times \exp\left\{j2\pi f_0 c^{-1} \vec{\vartheta} \left(\vec{r}_i' - \vec{r}_j'\right)\right\} d\vec{\vartheta} = 4\Delta F \dot{\Gamma}_{ij}(f_0), \quad (58) \end{aligned}$$

where, based on equations (7) and (8), we can write

$$\begin{aligned} \left\langle \dot{S}_1(\vec{\vartheta}_1, t) \dot{S}_2^*(\vec{\vartheta}_2, t) \right\rangle &= \\ &= 4\Delta F G\sigma^0(\vec{\vartheta}_1, f_0) \delta(\vec{\vartheta}_1 - \vec{\vartheta}_2), \quad (59) \end{aligned}$$

$$\begin{aligned} \dot{\Gamma}_{ij}(f_0) &= \int_{-\infty}^{\infty} G\sigma^0(\vec{\vartheta}, f_0) \dot{E}_{ai}(\vec{\vartheta}, f_0) \times \\ &\times \dot{E}_{aj}^*(\vec{\vartheta}, f_0) \exp\left\{j2\pi f_0 c^{-1} \vec{\vartheta} \left(\vec{r}_i' - \vec{r}_j'\right)\right\} d\vec{\vartheta}. \quad (60) \end{aligned}$$

The matrix of variable $\dot{\Gamma}_{ij}(f_0)$ is an indicator of the coherence degree of signals obtained at the outputs of AA elementary antennas. The obtained result coincides with the second part of equation (52) at frequencies $f = f_{0m}$. In this case, based on equations (51) and (60) at frequencies $f = f_{0m}$, we obtain the image estimation $G\sigma^0(\vec{\vartheta}_k, f)$ in the form of a discrete Fourier transform of these numbers. This is the step of the practical signal processing algorithm, i.e. formation of the spatial function of mutual coherence of complex analytical signals:

$$\begin{aligned} G\hat{\sigma}^0(\vec{\vartheta}_k, f) &= \sum_{i=1}^N \sum_{j=1}^N \dot{\Gamma}_{ij}(f_0) \exp\left[-j2\pi f_0 \frac{\vec{\vartheta}_k \left(\vec{r}_i' - \vec{r}_j'\right)}{c}\right] = \\ &= \frac{1}{4\Delta F} \sum_{i=1}^N \sum_{j=1}^N \left\langle \dot{S}(t, \vec{r}_i') \dot{S}^*(t, \vec{r}_j') \right\rangle \times \\ &\times \exp\left[-j2\pi f_0 \frac{\vec{\vartheta}_k \left(\vec{r}_i' - \vec{r}_j'\right)}{c}\right]. \quad (61) \end{aligned}$$

Formula (52) for the variables $\dot{\Gamma}_{ij}(f_0)$, expressed in terms of the coherence function and the mutual correlation function of the APD of elementary antennas $\dot{R}_{0ik(\text{APD})}(\cdot)$, we obtain as follows. We write the RPs product in the following form:

$$\begin{aligned} \dot{E}_{ai}(\vec{\vartheta}, f_0) \dot{E}_{aj}^*(\vec{\vartheta}, f_0) &= \int_{-\infty(D')}^{\infty} \int_{-\infty(D')}^{\infty} \dot{I}_{ai}(\vec{r}_1', f_0) \times \\ &\times \dot{I}_{aj}^*(\vec{r}_2', f_0) \exp\left\{j2\pi f_0 c^{-1} \vec{\vartheta} \left(\vec{r}_1' - \vec{r}_2'\right)\right\} d\vec{r}_1' d\vec{r}_2' = \\ &= \int_{-\infty(D')}^{\infty} \left\{ \int_{-\infty(D')}^{\infty} \dot{I}_{ai}(\vec{r}_1', f_0) \dot{I}_{aj}^*(\vec{r}_1' - \Delta\vec{r}', f_0) d\vec{r}_1' \right\} \times \\ &\times \exp\left\{j2\pi f_0 c^{-1} \vec{\vartheta} \Delta\vec{r}'\right\} d\Delta\vec{r}' = \int_{-\infty(D')}^{\infty} \dot{R}_{aij(\text{ADP})}(\Delta\vec{r}', f_0) \times \\ &\times \exp\left\{j2\pi f_0 c^{-1} \vec{\vartheta} \Delta\vec{r}'\right\} d\Delta\vec{r}'. \quad (62) \end{aligned}$$

Assuming the values of the integration limits to be sufficiently large, we neglect the influence of their changes upon the change of variables. We substitute equations (14) and (62) into (60). As a result, we obtain equation similar to (53):

$$\begin{aligned} \dot{\Gamma}_{ij}(f_0) &= \int_{-\infty}^{\infty} G\sigma^0(\bar{\vartheta}, f_0) \dot{E}_{ai}(\bar{\vartheta}, f_0) \dot{E}_{aj}^*(\bar{\vartheta}, f_0) \times \\ &\times \exp\left\{j2\pi f_0 c^{-1} \bar{\vartheta}(\bar{r}'_i - \bar{r}'_j)\right\} d\bar{\vartheta} = \int_{-\infty}^{\infty} \frac{f_0^2}{c^2} \int_{-\infty}^{\infty} \dot{\Gamma}_{\sigma}(f_0, \Delta\bar{r}'_1) \times \\ &\times \dot{R}_{aij(ADP)}(\Delta\bar{r}'_2, f_0) \times \\ &\times \int_{-\infty}^{\infty} \exp\left\{-j2\pi f_0 c^{-1} \bar{\vartheta} \left[\Delta\bar{r}'_1 - \Delta\bar{r}'_2 - (\bar{r}'_i - \bar{r}'_j)\right]\right\} d\bar{\vartheta} \Delta\bar{r}'_1 \Delta\bar{r}'_2 = \\ &= \int_{-\infty}^{\infty} \dot{\Gamma}_{\sigma}(f_0, \Delta\bar{r}') \dot{R}_{aij(ADP)}\left[f_0, \Delta\bar{r}' - (\bar{r}'_i - \bar{r}'_j)\right] \Delta\bar{r}' . \quad (63) \end{aligned}$$

The practical implementation of the algorithm for the coherence degree $\dot{\Gamma}_{ij}(f_0)$ obtaining can be carried out in accordance with an equation similar to (39) but considering the discrete form of the AA with the replacement of the integration operation by summation. Assuming the AA to be two-dimensional, we denote the positions of the phase centers of elementary antennas \bar{r}'_{nl} , $n = 1:N$, $l = 1:L$, and their output signals by double indices $\dot{S}(t, \bar{r}'_{nl})$. Then we obtain the algorithm for the formation of the coherence degree:

$$\begin{aligned} 4\Delta F \dot{\Gamma}_{ij}(f_{0m}) &= \left\langle \dot{S}(t, \bar{r}'_i) \dot{S}^*(t, \bar{r}'_j) \right\rangle \approx \\ &\approx \frac{1}{T_{NL}} \sum_{n=0}^{N-1} \sum_{l=0}^{L-1} \int_0^T \dot{S}(t, \bar{r}'_{nl}) \dot{S}^*(t, \bar{r}'_{n-i, l-j}) dt, \quad (62) \end{aligned}$$

where $\bar{r}'_{nl} - \bar{r}'_{n-i, l-j} = \Delta\bar{r}'_{ij}$.

Thus, to implement the second imaging algorithm by wideband active radars with AA and aperture synthesis it is necessary to perform the following algorithmic operations.

1. It is necessary to filter the spectrum of the received wideband signal into narrow frequency bands, in which the signals have close to constant spectral-correlation characteristics and satisfy the QMA conditions.

2. Next, it is necessary to obtain a set of the coherence degree values $\dot{\Gamma}_{ij}(f_{0m})$ on each frequency band in accordance with equation (64).

3. It is necessary to apply the discrete Fourier transform to the obtained values:

$$\sum_{i=1}^N \sum_{j=1}^L \dot{\Gamma}_{ij}(f_{0m}) \exp\left(-j2\pi f_{0m} \frac{\bar{\vartheta}_k \Delta\bar{r}'_{ij}}{c}\right),$$

$$\Delta\bar{r}'_{ij} = \bar{r}'_i - \bar{r}'_j.$$

Images obtained in different frequency bands must be summed.

Other variants of aperture synthesis are also possible, for example, by forming the second derivatives of the spatial coherence functions of ultrawideband signals [24]. However, these options require appropriate additional research.

Simulation results

Let us simulate the obtained practical imaging algorithm for wideband systems with active aperture synthesis. We assume that the antenna array of the system is square and consists of 25 elements. Each element in the simulation has the shape of a circle with a radius of 0.2 m. The distance between the adjacent elements was 0.8 m. The location of the elements on the AA is shown in Figure 2. The frequency range of the probing signal in the simulation is in the range from 22 GHz to 46 GHz, which corresponds to the capabilities of the modern radio element base.

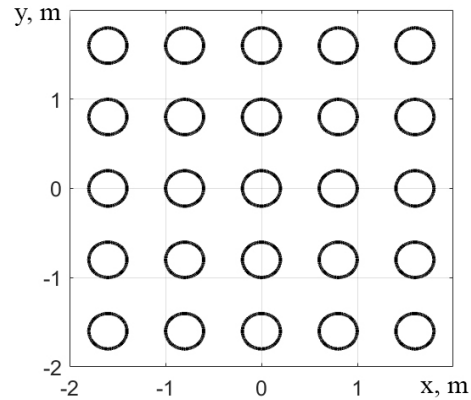


Fig. 2. Receiving antenna array geometry

The initial test image is taken from open sources and shown in Figure 3.

In accordance with the proposed imaging algorithm for a radar, it is initially necessary to filter the broadband probing signal into several narrow-band processes. Thus, in the simulation, the initial broadband process is divided into 600 subbands, the center frequencies of which start from 22.02 GHz and follow with a step of 40 MHz up to 45.98 GHz.



Fig. 3. Test image

Further, for the central frequency of each subband, the coherence degree value $\dot{\Gamma}_{ij}(f_{0m})$ is formed. While simulation, it is convenient to represent them by equation (63) as an integral of the product of the AF APD $\dot{R}_{aij(ADP)}[f_0, \Delta\vec{r}' - (\vec{r}'_i - \vec{r}'_j)]$ and the SDCSCF $\dot{\Gamma}_{\sigma}(f_0, \Delta\vec{r}')$. AF APD is calculated by equation (50), and SDCSCF can be represented by the Fourier transform of the test image. Figure 4 shows the modulus of the AF APD of the used antenna array on several different frequencies.

As can be seen in Figure 4, with an increase in frequency, the general form of the AF APD does not change, but its lobes expand and the distance between them increases.

The spectral representation of the test image, which is the function $\dot{\Gamma}_{\sigma}(f_0, \Delta\vec{r}')$, is shown in Figure 5.

Next, we obtain primary radar images at the central frequencies of each of the subbands. It is realized by applying the Fourier transform to the product $\dot{R}_{aij(ADP)}[f_0, \Delta\vec{r}' - (\vec{r}'_i - \vec{r}'_j)]$ on $\dot{\Gamma}_{\sigma}(f_0, \Delta\vec{r}')$ in each of the subbands. Images obtained in several subbands are shown in Figures 6, 7.

Primary radioimage is obtained according to equation (54) by summing 600 images of each frequency subbands. It is shown in Figure 8.

The obtained summary primary radio image in Figure 8 is detailed in compare with images obtained in individual subbands in Fig. 6. Thus, in Fig. 7, there is much more detail in the areas of roads, shed and grass. Obtained image quality can be significantly improved at the post-processing stage by applying decorelating or other types of filters [30, 31].

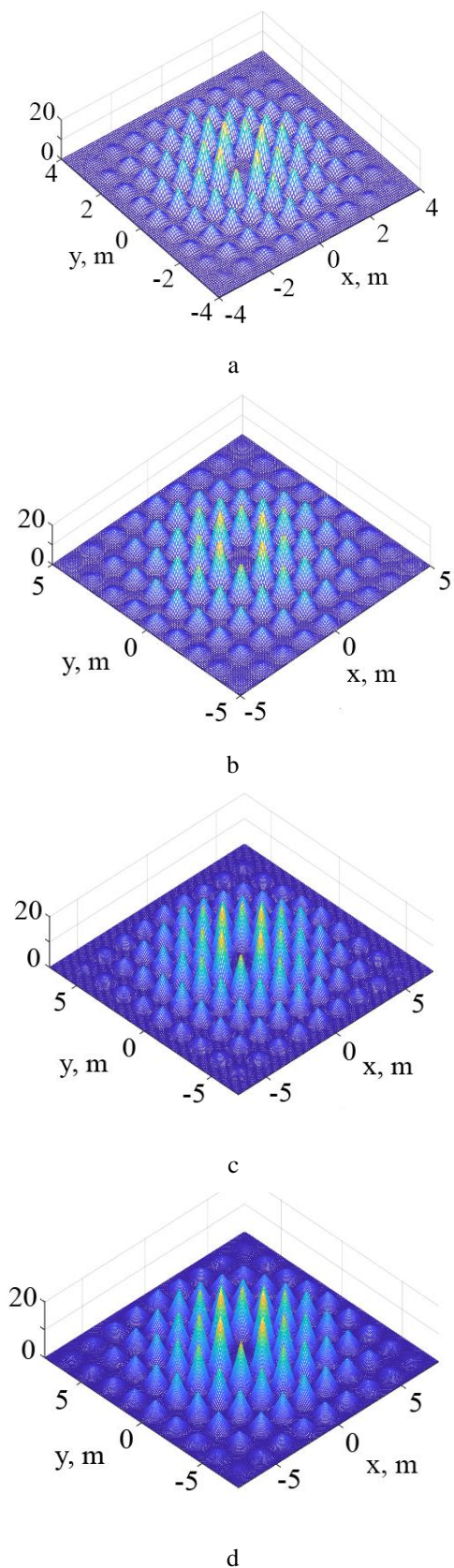


Fig. 4. Autocorrelation function of antenna array APD at 22.02 GHz (a), 30 GHz (b), 38 GHz (c) and 45.98 GHz (d)

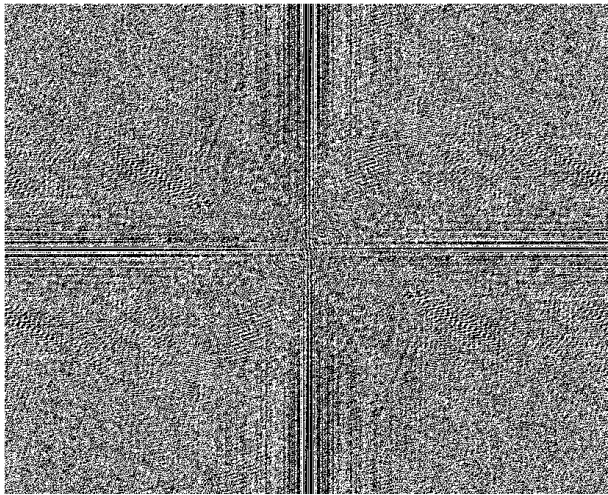
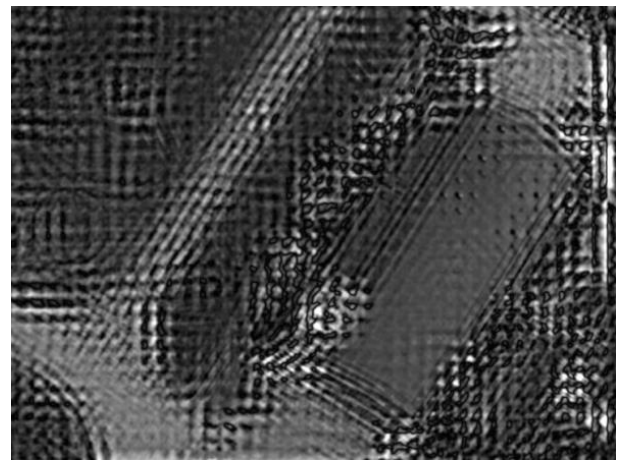


Fig. 5. Spectral density of the complex spatial coherence function for simulation

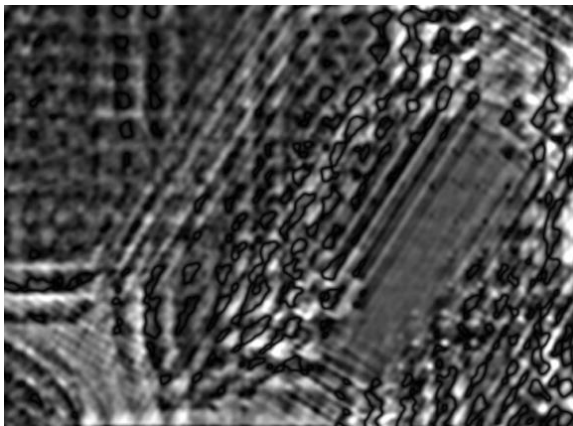


a

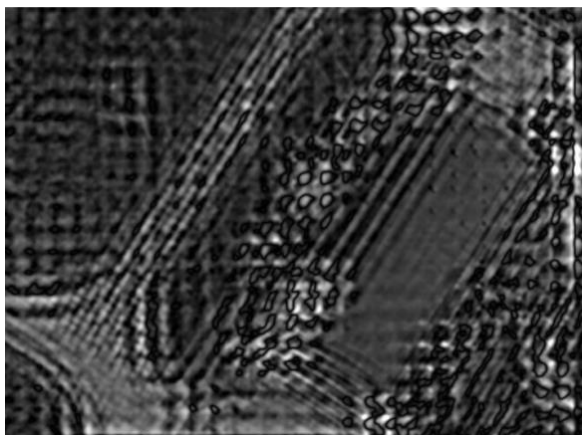


b

Fig. 7. Primary radar image obtained on center frequencies 38 GHz (a) and 45.98 GHz (b)



a



b

Fig. 6. Primary radar image obtained on center frequencies 22.02 GHz (a), 30 GHz (b)

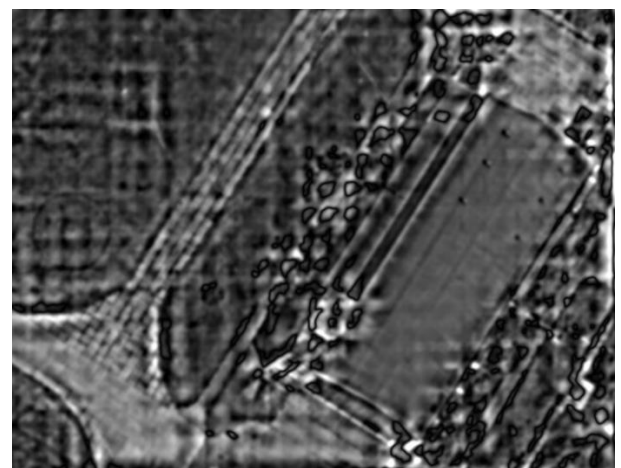


Fig. 8. Cross-correlation function of basic APD of elementary antennas of AA

However, of particular interest to improve the detailization of the obtained images is the optimization of the antenna array shape. Thus, the proposed system of active aperture synthesis is close to passive systems

used in radio astronomy. The quality of radio images obtained in radio astronomy multi-antenna systems significantly depends on the location of individual antenna elements in AA [32, 33]. In such systems, square arrays

with equidistant elements are extremely rarely used due to their low efficiency. Therefore, to improve the quality of the images obtained by the developed algorithm, in the future it is planned to conduct additional research to find more optimal options for the location of individual elements in an antenna array.

Experimental research

The imaging algorithms (47) and (55) are based on filtering the broadband signal into narrow frequency bands. Furthermore, the correlation processing of the signals is performed only on the central frequencies of each band. Therefore, it is advisable to investigate in practice how the correlation function of signals coherently received by several receivers changes, if instead of processing the entire frequency band, only the processing at some central frequency is performed. For this, in the anechoic chamber of the National Aerospace University "Kharkiv Aviation Institute" a stand has been created, that made it possible to investigate the effect of such processing on the measurement results.

The developed stand consists of transmitting and receiving parts. The receiving part is shown in Figure 9. SatIntegral T-031 satellite converters operating in the 3 cm. wavelength range are used as receivers. Each of these converters uses a built-in local oscillator based on a phase-locked loop to convert the received signal to an intermediate frequency. For the experiment, it is necessary to ensure the coherence of signal reception by individual receivers. This is performed by synchronizing the PLL of different converters by one external reference signal source (Figure 9, b) [34].

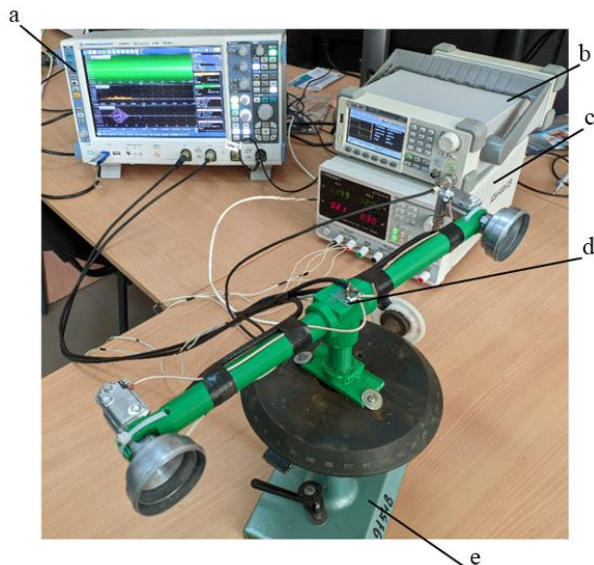


Fig. 9. Receiving part, where a) is an R&S RTO2044 oscilloscope; b) is the signal generator Siglent SDG5162; c) is the Siglent SPD3303C power supply unit; d) is chassis with receivers; e) is an automatic rotary device

To calculate the correlation coefficient between the received signals, the outputs of the receivers were connected via cables of the same length to a wideband oscilloscope R&S RTO2044 (Figure 9, a) with an operating frequency band of 5 GHz. Changing the delay time of the signal received by different receivers was implemented by turning them relative to the target direction.

A noise signal transmission part is shown in Figure 10. A GSHP-1 diode noise generator (Figure 10, c) was used to generate a noise probing signal with a band of 500 MHz. Since the generated signal power is quite low, amplifiers M421102-1 and M42152-2 were additionally used. To generate a monochromatic probing signal, instead of amplifiers and a noise generator, an R&S SMB100A generator connected to the transmission horn antenna was used.

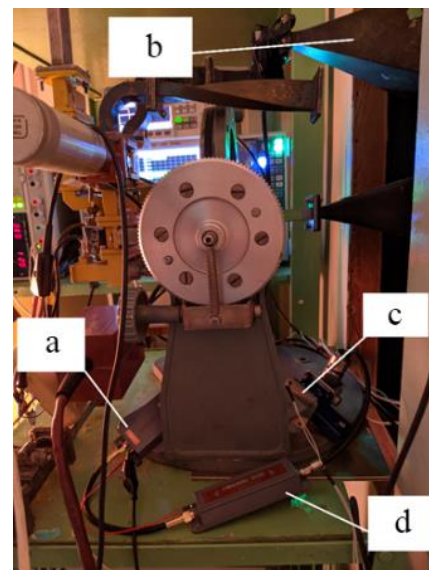


Fig. 10. Noise generation part, where a) is the amplifier M421102-1; b) is a transmission horn antenna; c) the generator section based on noise generator GSHP-1; d) is the amplifier M42152-2

During the experiment, a rotary device with receivers was installed in an anechoic chamber under a transmitting antenna (Figure 11).

A flat square reflector with a calculated EPR of 0.5 m², hung opposite the transmitting antenna, was used as a target.

During the first experiment, for the case of a monochromatic probing signal, a graph of the dependence of the correlation coefficient of the signals received by two receivers depending on their rotation relative to the target direction has been obtained. For this, the SMB100A generator was set to a frequency of 10.25 GHz. At the output of the receivers, there was an oscillation with a frequency of 500 MHz, which can be seen in the spectrum of the output signals in Figure 12. Figure 13 shows the shape of the received signals for the case when the receivers were directed exactly at the target.

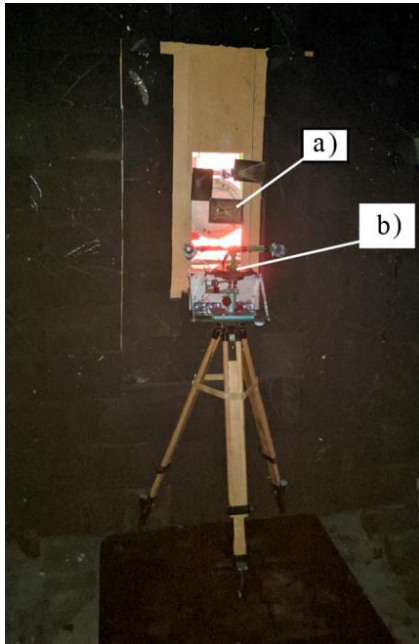


Fig. 11. The stand in an anechoic chamber, where a) is transmitting horn antenna; b) are receivers and automatic rotary device

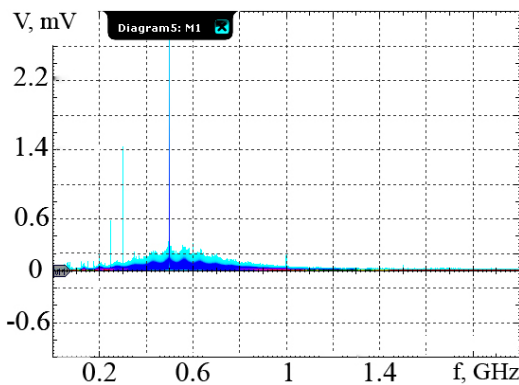


Fig. 12. Spectrum of receiver output signals for the case of monochromatic oscillation

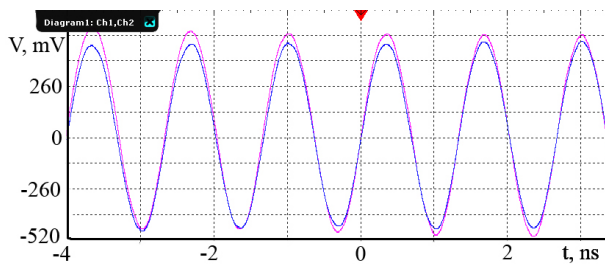


Fig. 13. Oscillograms of received signals for the case of monochromatic oscillation

The rotation of the receivers relative to the direction of the square reflector was carried out within the angles $\pm 90^\circ$. During rotation, the oscilloscope calculated the correlation coefficient of the received signals by

multiplying the two signals and calculating the average value. As a result, the dependence of the correlation coefficient of the receivers output signals on their angular position has been obtained. This is shown in Figure 14.

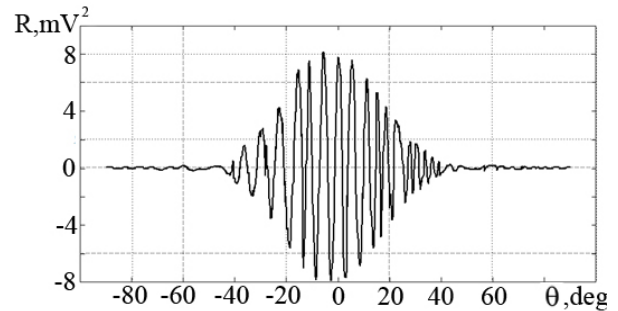


Fig. 14. Correlation coefficient depending on the angle of receiving system rotation for the case of a monochromatic signal

The resulting graph (Figure 14) corresponds to the theoretical statements. It has a periodic character. The attenuation of the amplitude relative to the center is due to the influence of a RP of the receivers (the square reflector goes beyond the RP).

During the next experiment, a noise signal with an approximate frequency band of 500 MHz was used as a probe. Figure 15 shows the spectrogram of the received noise signal.

As can be seen in Figure 15, the most powerful spectral components were in the range from 400 MHz to 900 MHz. That is, GSHP-1 generated noise approximately in the frequency range from 10.15 GHz to 10.65 GHz. Next, by analogy with the monochromatic signal, a graph of the correlation coefficient dependence of the received signals has been obtained. The resulting graph is shown in Figure 16.

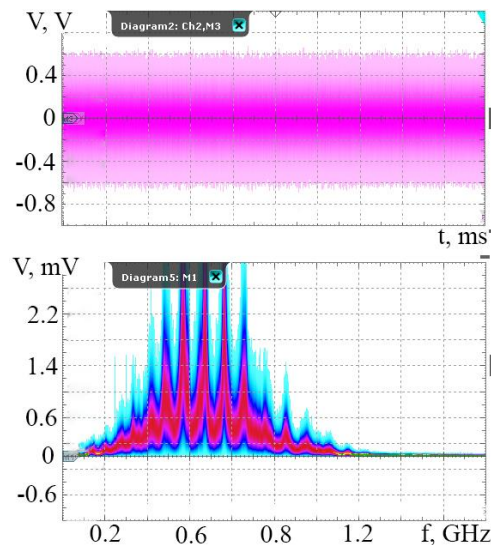


Fig. 15. Signals at the outputs of receivers and their spectrum for a case of noise probing signal

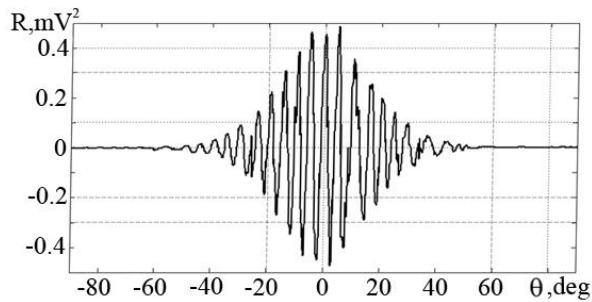


Fig. 16. Correlation coefficient of signals depending on the receiving system angle of rotation for the case of a signal with a band of 500 MHz

To compare the obtained results, we plot the dependences of the correlation coefficients for wideband and monochromatic signals on the same graph, having previously normalized them. The resulting plot is shown in Figure 17. θ

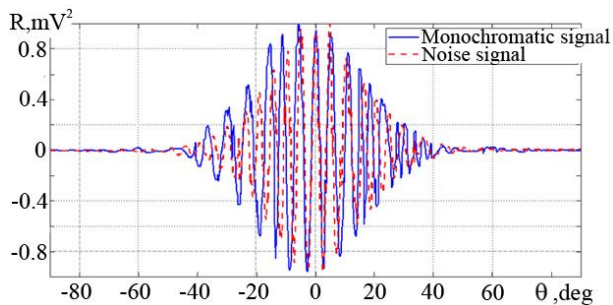


Fig. 17. Normalized correlation functions for cases of monochromatic and noisy probing signals

Analyzing the results in Figure 17, we can make two important conclusions. First, the expansion of the processing frequency band narrows the obtained characteristic and accelerates the fading of its side lobes. It can be argued that with further expansion of the noise frequency band, the function will take on an almost single-lobed form. This will allow to increase the resolution of the obtained images, provided that the entire frequency band is simultaneously processed. To test this theory in the future, it is planned to develop an aperture synthesis system with wideband receivers and a wideband noise signal source.

On the other hand, the obtained result confirms the van Cittert-Zernike theorem. That is, in the case of a non-broadband signal processing, it is advisable to perform processing only at the central frequency of a signal. Thus, the obtained plots do not have a significant difference, which allows you to perform processing not in the entire frequency band, but only at its central frequency. This confirms the general efficiency of the proposed algorithms (46) and (54), which involve filtering a broadband signal into several narrowband ones.

Conclusions

In this paper, we propose new algorithms for incoherent imaging in active radars with ultra-wideband stochastic probing signals and antenna arrays. Signal processing is based on methods close to aperture synthesis methods, which are common in passive radio-metric systems of astronomy and remote sensing. A mathematical description of two methods of explicit and implicit focusing of antenna systems on the underlying surface elements is given. With explicit focusing, it is necessary to equalize the phases, to sum the signals in phase at each signal frequency, to measure their power, and to sum the resulting images. With implicit focusing, after filtering the received signal spectrum into narrow frequency bands, images are obtained by forming complex coherence functions and applying spatial Fourier transforms to them. A complete mathematical substantiation of these methods is given in relation to modern active radars.

Because of the simulation, the overall performance of the obtained practical algorithm for radar imaging is confirmed. Primary images are obtained for different frequency ranges when a signal is processed only at the center frequency of each range. A summary radio image was also calculated.

The correlation functions of broadband and monochromatic signals received by diversity antennas were experimentally studied. It is shown that when processing a relatively non-wideband signal, it is advisable to process it at its central frequency, rather than the process the entire frequency band. Thus, the differences between the obtained correlation functions for the two mentioned cases are insignificant.

The obtained results are of considerable interest for solving the problems of radar images obtained from aerospace carriers at probing angles close to the vertical. Therefore, in the specified field of view, classical synthetic aperture radars cannot provide a high-resolution radar image.

Further research in this direction will be focused on the development of active radar with aperture synthesis and experimental forming of radar images using the obtained algorithms.

Contribution of authors: conceptualization – Simeon Zhyla, Valerii Volosyuk, Vladimir Pavlikov; methodology – Valerii Volosyuk, Simeon Zhyla; simulation – Simeon Zhyla, Tatyana Nikitina; conducting the experiment – Anatoliy Popov, Oleksandr Shmatko, Eduard Tserne; validation – Olena Havrylenko, Nataliia Kuzmenko; formal analysis – Borys Kuznetsov, Yuliya Averyanova; investigation – Nikolay Ruzhentsev, Olga Sushchenko; resources – Maksym Zaliskyi, Oleksandr Solomentsev; data cura-

tion – **Ivan Ostroumov**; writing- original draft – **Eduard Tserne, Valerii Volosyuk**; writing-review and editing – **Kostiantyn Dergachov, Ivan Ostroumov**; supervision – **Valerii Volosyuk**; project administration – **Eduard Tserne**; funding acquisition – **Simeon Zhyla**.

All authors have read and agreed to the published version of the manuscript.

Acknowledgement. The work has been funded by the Ministry of Education and Science of Ukraine. The state registration number of the project «Development of the theory of ultra-wideband active aperture synthesis systems for high-precision remote sensing from high-speed aero-space platforms» is 0119U100968.

Project information. The project 0119U100968 is devoted to the development of the statistical synthesis theory of ultra-wideband systems and methods for radio imaging from aerospace carriers. The main purpose of the project is to develop the theory and bases of technical implementation of ultra-wideband radars for high-precision mapping of the underlying surface in the "blind zone" (-15° to $+15^\circ$ from nadir) of the classical surveillance radio-systems. The peculiarity of the developed theory is to combine the methods of active and passive radar, modern achievements of bootstrap analysis of signals and spectral methods of super-resolution.

The project is based on the approach of a constructive combination of mathematical methods of statistical theory of radio systems synthesis and heuristic methods of system development. Their combination has allowed to develop a new type of radio systems (radio complexes). It is systems with active aperture synthesis. Another feature of the theory obtained is that it does not impose any restrictions on the signal band of the implemented systems. This made it possible to synthesize the algorithms for the processing of stochastic wideband signals to perform a high-precision imaging in the observation angles from -15° to $+15^\circ$ of the direction to nadir.

In addition, several new results related to the theory of wideband signals processing have been obtained during the performance of the project. This is a consequence of the combination of mathematical methods of signal processing obtained in the process of developing the theory of ultra-wideband radio systems. The methods developed in the project allow us to implement not abstract mathematical algorithms, but structures of complete radio systems. They can work in a wide range of conditions of use, which is important for the creation of civilian and military systems. In addition to mathematical methods of radio systems design, the processing methods (inverse filtration of primary radioimages) are obtained in the project, which will allow increase the images resolution (secondary radioimages). These methods are obtained during the solution of inverse

tasks (searching for the special filters core, reverse to those that are included to integral equations during optimization).

References

1. Chang, C. Y., Woo, A., Forry, H., Sherman, J., Recht, M., Clark, R. and Levin, R. HISAR-300: an advanced airborne multi-mission surveillance radar. *IEEE Radar Conference (RadarConf-2019)*, 2019, pp. 1-16. DOI: 10.1109/RADAR.2019.8835599.
2. Taylor, C D., et al. Airborne Dual-Band Microwave Radar System for Snow Thickness Measurement. *IEEE International Geoscience and Remote Sensing Symposium (IGARSS 2020)*, 2020, pp. 2934-2937. DOI: 10.1109/IGARSS39084.2020.9323958.
3. Lorente, D., Limbach, M. and Gabler, B. L-Band Antenna Array for Next Generation DLR Airborne SAR Sensor. *12th German Microwave Conference (GeMiC-2019)*, 2019, pp. 182-185. DOI: 10.23919/GEMIC.2019.8698151.
4. Zhyla, S., et al. Time-frequency representation enhancement: approach based on image filtering methods. *Radioelectronic and Computer Systems*, 2022, no. 1, pp. 178-194. DOI: 10.32620/reks.2022.1.14.
5. Wang, D. Gm-Compensated 46-101 GHz Broadband Power Amplifier for High-Resolution FMCW Radars. *IEEE International Symposium on Circuits and Systems (ISCAS-2021)*, 2021, pp. 1-5. DOI: 10.1109/ISCAS51556.2021.9401773.
6. Zhang, L., Kuang, Q., Chang, M. and Zhang, D. 10-GS/s Sample and Hold System for High-Speed Time-Interleaved ADC. *Eighth International Conference on Instrumentation & Measurement, Computer, Communication and Control (IMCCC-2018)*, 2018, pp. 705-708. DOI: 10.1109/IMCCC.2018.00152.
7. Chernyshev, S. and Vilenskiy, A. Formation and Processing of Noise-Like Signals in Ultra-Wideband Systems. *XXI International Conference Complex Systems: Control and Modeling Problems (CSCMP-2019)*, 2019, pp. 664-666. DOI: 10.1109/CSCMP45713.2019.8976577.
8. Arnauti, El- G., Saalman, O. and Brenner A. R. Ultra-high resolution airborne experiments with a new Ka-band SAR sensor. *European Radar Conference (EURAD-2017)*, 2017, pp. 409-412. DOI: 10.23919/EURAD.2017.8249234.
9. Wei, L., Wijnholds, S. J. and Hurley, P. Robust recovery for aperture synthesis imaging. *IEEE International Conference on Image Processing (ICIP-2017)*, 2017, pp. 3570-3574. DOI: 10.1109/ICIP.2017.8296947.
10. Schooneveld, V. C. *Image Formation from Coherence Functions in Astronomy*. Berlin, Springer Publ., 1987. 340 p.

11. Morrison, R. L. and Phelps, E. B. Radio Astronomy Techniques for Multistatic Radar Imaging and Localization of Space Objects. *International Applied Computational Electromagnetics Society Symposium. (ACES-2019)*, 2019, pp. 1-2.
12. Kraus, T., Krieger, G., Bachmann, M. and Moreira, A. Formation Considerations for Distributed Satellite SAR Systems. *13th European Conference on Synthetic Aperture Radar. (EUSAR-2021)*, 2021, pp. 1-6.
13. Fang, T., Deng, Y., Liang, D., Zhang, L., Zhang, H. and Fan, H. Multichannel Sliding Spotlight SAR Imaging: First Result of GF-3 Satellite. *IEEE International Geoscience and Remote Sensing Symposium. (IGARSS-2020)*, 2020, pp. 1925-1928. DOI: 10.1109/IGARSS39084.2020.9323296.
14. Li, Q., Feng, L., Wang, H., Zheng, S., Wu, S. and Sun, Z. Research on Sliding spotlight imaging algorithm. *3rd China International SAR Symposium. (CISS-2022)*, 2022, pp. 1-5. DOI: 10.1109/CISS57580.2022.9971246.
15. Kendra, J. R., Bloy, G. J. and Hughes, J. Rotary-Motion-Extended Array Synthesis (R-MXAS): Simultaneous Sparsity and Sensitivity in a Synthetic Aperture Imaging Radiometer. *IEEE International Geoscience and Remote Sensing Symposium. (IGARSS-2021)*, 2021, pp. 7696-7699. DOI: 10.1109/IGARSS47720.2021.9554144.
16. Fu, P., Hu, F., Hu, H. and Zheng, T. A Wave-number Domain Imaging Algorithm for Synthetic Aperture Interferometric Radiometry in Near-Field. *IEEE International Geoscience and Remote Sensing Symposium. (IGARSS-2020)*, 2020, pp. 6511-6514. DOI: 10.1109/IGARSS39084.2020.9323395
17. Mytsenko, I., Pedenko, Y., Kabanov, V. and Roenko, A. A Passive-Active Radar with Channels Operating Simultaneously on Common Antenna. *IEEE Ukrainian Microwave Week. (UkrMW-2020)*, 2020, pp. 1-4. DOI: 10.1109/UkrMW49653.2020.9252752.
18. Brzozowski, M., Pakowski, M., Jakielaszek, Z., Michalczewski, M. and Myszka, M. A Challenges of preparation and realization of combined field tests of passive and active radar sensors on an example APART-GAS 2019 trials. *IEEE 8th International Workshop on Metrology for AeroSpace. (MetroAeroSpace-2021)*, 2021, pp. 188-192. DOI: 10.1109/MetroAeroSpace51421.2021.9511746.
19. Gromek, D., Samczyński, P., Radecki, K., Drozdowicz, J. and Stasiak, K. Challenges of preparation and realization of combined field tests of passive and active radar sensors on an example APART-GAS 2019 trials. *21st International Radar Symposium. (IRS-2020)*, 2020, pp. 240-244. DOI: 10.23919/IRS48640.2020.9253903.
20. Fränken, D. and Liegl, A. Integration of Multi-Band Passive and Multi-Functional Active Radar Data. *IEEE Radar Conference. (RadarConf22)*, 2022, pp. 1-6. DOI: 10.1109/RadarConf2248738.2022.9764215.
21. Pavlikov, V. *Rozvytok teoriiy syntezu ta analizu system aktyvnogo aperturnogo syntezu pry kartografuvanni poverxni u dalnij zoni* [Development of the theory of ultra wideband active aperture synthesis systems for high-precision remote sensing from highspeed aerospace platforms]. Nat. Aerosp. University «Kharkiv Aviation Institute» Publ., 2020. 125 p.
22. Volosyuk, V. K., et al. Mathematical description of imaging processes in ultra-wideband active aperture synthesis systems using stochastic sounding signals. *Radioelectronic and Computer Systems*, 2021, no. 4, pp. 166-182. DOI: 10.32620/REKS.2021.4.14.
23. Pavlikov, V., Volosyuk, V., Zhyla, S., Tserne, E., Shmatko, O., Sobkolov, A. Active-Passive Radar for Radar Imaging from Aerospace Carriers. *IEEE 19th International Conference on Smart Technologies (EUROCON)*, 2021, pp. 18-24. DOI: 10.1109/EUROCON52738.2021.9535619.
24. Volosyuk, V. K., Kravchenko, V. F. *Statisticheskaya teoriya radiotekhnicheskikh sistem distantsionogo zondirovaniya i radiolokatsii* [Statistical Theory of Radio-Engineering Systems of Remote Sensing and Radar]. Moscow, Fizmatlit Publ., 2008. 704 p.
25. Carozzi, T. D. and Woan, G. A generalized measurement equation and van Cittert-Zernike theorem for wide-field radio astronomical interferometry. *Monthly Notices of the Royal Astronomical Society*, 2021, no. 3(395), pp. 1558-1568. DOI: 10.1111/j.1365-2966.2009.14642.x.
26. Marr, J. M., Snell, R. L. and Kurtz, S. E. *Fundamentals of radio astronomy. Observational methods*. Boca Raton, CRC Press Publ., 2016. 350 p.
27. Condon, J. J. and Ransom S. M. *Essential Radio Astronomy*. Princeton, Princeton University Press Publ., 2016. 376 p.
28. Philippe, B. and Reynaert, P. A Quadrature Phase Detector in 28nm CMOS for Differential mm-Wave Sensing Applications Using Dielectric Waveguides. *IEEE 44th European Solid State Circuits Conference (ESSCIRC 2018)*, 2018, pp. 114-117. DOI: 10.1109/ESSCIRC.2018.8494306.
29. Zougari, B., Hammou, D., Hannachi, C. and Tatu, S. O., High Dynamic Range Low Power Drive Quadrature Millimeter-Wave Demodulator. *48th European Microwave Conference (EuMC-2018)*, 2018, pp. 255-258. DOI: 10.23919/EuMC.2018.8541411.
30. Arienzo, A., Argenti, F. and Alparone, L. Impact of a Spatial Decorrelation of the Noise on the Performance of Despeckling Filters for Polarimetric SAR Data. *Photonics & Electromagnetics Research Sympos-*

sium (PIERS-Spring 2019), 2019, pp. 1113-1121. DOI: 10.1109/PIERS-Spring46901.2019.9017856

31. Zemliachenko, O. N., Ivakhnenko, I. G., Chernova, G.A. and Lukin, V. V. Analysis of opportunities to improve image denoising efficiency for dct-based filter. *Radioelectronic and Computer Systems*, 2018, no. 2, pp. 4-12. DOI: 10.32620/reks.2018.2.01.

32. Cappellen, W. A. and Ardenne, A. Development of mid-frequency aperture arrays for radio astronomy. *IEEE Radio and Antenna Days of the Indian Ocean (RADIO-2017)*, 2018, pp. 1-2. DOI: 10.23919/RADIO.2017.8242214.

33. Hall, P. J., Benthem, P. and Sutinjo, A. T. Aperture array verification system 1: Overview of a square kilometre array prototype. *International Conference on Electromagnetics in Advanced Applications (ICEAA-2016)*, 2016, pp. 345-348. DOI: 10.1109/ICEAA.2016.7731394.

34. *Phase Synchronization of Multiple PLL Synthesizers. Reference Design*. Texas Instruments Incorporated, 2017. Available at: <https://www.ti.com/lit/pdf/tidud11> (accessed 08 January 2023).

Надійшла до редакції 10.01.2023, розглянута на редколегії 20.02.2023

ПРАКТИЧНІ АЛГОРИТМИ ФОРМУВАННЯ ЗОБРАЖЕНЬ У НАДШИРОКОСМУГОВИХ РАДІОЛОКАЦІЙНИХ СИСТЕМАХ АКТИВНОГО АПЕРТУРНОГО СИНТЕЗУ З ВИКОРИСТАННЯМ СТОХАСТИЧНИХ ЗОНДУЮЧИХ СИГНАЛІВ

*Семен Жила, Валерій Волосюк, Володимир Павліков,
Микола Руженцев, Едуард Церне, Анатолій Попов, Олександр Шматко, Олена Гавриленко,
Наталія Кузьменко, Костянтин Дергачов, Юлія Авер'янова,
Ольга Сущенко, Максим Заліський, Олександр Соломенцев,
Іван Остроумов, Борис Кузнецов, Тетяна Нікітіна*

Предметом дослідження є алгоритми формування радіолокаційних зображень. **Мета** роботи полягає у розробці методів формування зображень ширококуговими та надширококуговими системами активного апертурного синтезу, що використовують антенні решітки та стохастичні зондуючі сигнали. Використання антенних решіток дозволяє отримати радіолокаційне зображення без необхідності переміщення системи у просторі. Водночас використання ширококугових зондувальних сигналів обґрунтовано їх вузькими автокореляційними функціями, що дозволяє покращити роздільну здатність сформованих зображень. Основна **ідея** запропонованих алгоритмів полягає у розфільтруванні вихідного ширококугового сигналу на кілька вузькосмугових процесів. Подальша обробка передбачається тільки на центральних частотах кожного з цих процесів. Такий підхід дозволяє для випадку ширококугового сигналу використовувати класичні поширені методи апертурного синтезу, які можуть застосовуватися тільки для вузькосмугових сигналів, що задовольняють умові квазімонохроматичного наближення. Це значно зменшує загальну обчислювальну складність алгоритму формування зображень, що спрощує подальшу практичну реалізацію відповідної системи на існуючій елементній базі. В результаті імітаційного моделювання сформовано первинне радіолокаційне зображення і підтверджено загальну працездатність запропонованого підходу до обробки ширококугових процесів. Показано підвищення якості зображення, що формується при використанні декількох частотних діапазонів. Виконано експериментальне дослідження впливу обробки ширококугового сигналу тільки на його центральній частоті замість усієї смуги частот на прикладі побудови кореляційної функції сигналів, прийнятих двома рознесеними приймачами. В результаті, експериментально підтверджені викладки теореми Ван Циттерта-Цернике, яка допускає обробку сигналу тільки на його центральній частоті замість всієї смуги частот. Одночасно визначено перспективність розширення смуги зондувального сигналу, що за наявності ширококугової елементної бази та пристроїв високошвидкісної обробки інформації дозволить додатково підвищити роздільну здатність системи.

Ключові слова: активний апертурний синтез; формування зображень за допомогою радару; ширококугові системи; кореляційні функції.

Жила Семен Сергійович – д-р техн. наук, зав. каф. аерокосмічних радіоелектронних систем, Національний аерокосмічний університет ім. М. С. Жуковського «Харківський авіаційний інститут», Харків, Україна.

Волосюк Валерій Костянтинович – д-р техн. наук, проф., проф. каф. аерокосмічних радіоелектронних систем, Національний аерокосмічний університет ім. М. Є. Жуковського «Харківський авіаційний інститут», Харків, Україна.

Павліков Володимир Володимирович – д-р техн. наук, проф., проректор з наукової роботи, Національний аерокосмічний університет ім. М. Є. Жуковського «Харківський авіаційний інститут», Харків, Україна.

Руженцев Микола Вікторович – д-р техн. наук, проф., головний наук. співроб. каф. аерокосмічних радіоелектронних систем, Національний аерокосмічний університет ім. М. Є. Жуковського "Харківський авіаційний інститут", Харків, Україна.

Церне Едуард Олексійович – ас. каф. аерокосмічних радіоелектронних систем, Національний аерокосмічний університет ім. М. Є. Жуковського "Харківський авіаційний інститут", Харків, Україна.

Попов Анатолій Владиславович – д-р техн. наук, доц., доц. каф. аерокосмічних радіоелектронних систем, Національний аерокосмічний університет ім. М. Є. Жуковського "Харківський авіаційний інститут", Харків, Україна.

Шматко Олександр Олександрович – канд. техн. наук, старш. наук. співроб., Національний аерокосмічний університет ім. М. Є. Жуковського «Харківський авіаційний інститут», Харків, Україна.

Гавриленко Олена Володимирівна – канд. техн. наук, доц. каф. систем управління літальних апаратів., Національний аерокосмічний університет ім. М.Є. Жуковського "Харківський авіаційний інститут", Харків, Україна.

Кузьменко Наталія Сергіївна – канд. техн. наук, старш. наук. співроб. каф. аеронавігаційних систем, Національний авіаційний університет, Київ, Україна.

Дергачов Костянтин Юрійович – канд. техн. наук, зав. каф. систем управління літальних апаратів, Національний аерокосмічний університет ім. М. Є. Жуковського "Харківський авіаційний інститут", Харків, Україна.

Авер'янова Юлія Анатоліївна – д-р техн. наук, доц., проф. каф. аеронавігаційних систем, Національний авіаційний університет, Київ, Україна.

Сущенко Ольга Андріївна – д-р техн. наук, проф., проф. каф. аерокосмічних систем управління, Національний авіаційний університет, Київ, Україна.

Заліський Максим Юрійович – д-р техн. наук, доц., проф. каф. телекомунікаційних систем, Національний авіаційний університет, Київ, Україна.

Соломенцев Олександр Васильович – д-р техн. наук, проф., проф. каф. телекомунікаційних систем, Національний авіаційний університет, Київ, Україна.

Остроумов Іван Вікторович – д-р техн. наук, доц., проф. каф. аеронавігаційних систем, Національний авіаційний університет, Київ, Україна.

Кузнецов Борис Іванович – д-р техн. наук, проф., зав. відділу проблем управління магнітним полем, Державна установа «Інститут технічних проблем магнетизму Національної академії наук України», Харків, Україна.

Нікітіна Тетяна Борисівна – д-р техн. наук, проф., зав. каф. природничих і гуманітарних дисциплін, Харківський національний автомобільно дорожній університет, Харків, Україна.

Simeon Zhyla – D.Sc. in Radioengineering, Head of Aerospace Radio-electronic Systems Department, National Aerospace University "Kharkiv Aviation Institute", Kharkiv, Ukraine, e-mail: s.zhyla@khai.edu, ORCID: 0000-0003-2989-8988.

Valerii Volosyuk – D.Sc. in Radioengineering, Professor of Aerospace Radio-electronic Systems Department, National Aerospace University "Kharkiv Aviation Institute", Kharkiv, Ukraine, e-mail: v.volosyuk@khai.edu, ORCID: 0000-0002-1442-6235.

Vladimir Pavlikov – D.Sc. in Radioengineering, Professor, Vice rector for Science, National Aerospace University "Kharkiv Aviation Institute", Kharkiv, Ukraine, e-mail: v.pavlikov@khai.edu, ORCID: 0000-0002-6370-1758.

Nikolay Ruzhentsev – D.Sc. in Radioengineering, Professor, Chief Researcher of Aerospace Radio-electronic Systems Department, National Aerospace University "Kharkiv Aviation Institute", Kharkiv, Ukraine, e-mail: nvruzh@gmail.com, ORCID: 0000-0003-3023-4927.

Eduard Tserne – Assistant of Aerospace Radio-Electronic Systems Department, National Aerospace University "Kharkiv Aviation Institute", Kharkiv, Ukraine,
e-mail: e.tserne@khai.edu, ORCID: 0000-0003-0709-2238.

Anatoliy Popov – D.Sc. in Radioengineering, Associate Professor of Aerospace Radio-Electronic Systems Department, National Aerospace University "Kharkiv Aviation Institute", Kharkiv, Ukraine,
e-mail: a.v.popov@khai.edu, ORCID: 0000-0003-0715-3870.

Oleksandr Shmatko – PhD in Radioengineering, Senior Researcher, Laboratory of electron microscopy, optics, and laser technologies, National Aerospace University "Kharkiv Aviation Institute", Kharkiv, Ukraine,
e-mail: o.shmatko@khai.edu, ORCID: 0000-0002-3236-0735.

Olena Havrylenko – PhD in Engineering, Associate Professor, Aircraft Control Systems Department, National Aerospace University "Kharkiv Aviation Institute", Kharkiv, Ukraine,
e-mail: o.havrylenko@khai.edu, ORCID: 0000-0001-5227-9742.

Nataliia Kuzmenko – PhD in Engineering, Senior Researcher of Air Navigation Systems Department, National Aviation University, Kyiv, Ukraine,
e-mail: nataliiakuzmenko@ukr.net, ORCID: 0000-0002-1482-601X.

Kostiantyn Dergachov – PhD in Engineering, Associate Professor, Head of Aircraft Control Systems Department, National Aerospace University "Kharkiv Aviation Institute" Kharkiv, Ukraine,
e-mail: k.dergachov@khai.edu, ORCID: 0000-0002-6939-3100.

Yuliya Averyanova – D.Sc. in Engineering, Associate Professor, Professor of Air Navigation Systems Department, National Aviation University, Kyiv, Ukraine,
e-mail: ayua@nau.edu.ua, ORCID: 0000-0002-9677-0805.

Olga Sushchenko – D.Sc. in Engineering, Professor, Professor of Aerospace Control Systems Department, National Aviation University, Kyiv, Ukraine,
e-mail: sushoa@ukr.net, ORCID: 0000-0002-8837-1521.

Maksym Zaliskyi – D.Sc. in Engineering, Associate Professor, Professor of Telecommunication and Radioelectronic Systems Department, National Aviation University, Kyiv, Ukraine,
e-mail: maximus2812@ukr.net, ORCID: 0000-0002-1535-4384.

Oleksandr Solomentsev – D.Sc. in Engineering, Professor, Professor of Telecommunication and Radioelectronic Systems Department, National Aviation University, Kyiv, Ukraine,
e-mail: avsolomentsev@ukr.net, ORCID: 0000-0002-3214-6384.

Ivan Ostroumov – D.Sc. in Engineering, Associate Professor, Professor of Air Navigation Systems Department, National Aviation University, Kyiv, Ukraine,
e-mail: ostroumovv@ukr.net, ORCID: 0000-0003-2510-9312.

Borys Kuznetsov – D.Sc. in Engineering, Professor, Head of Magnetic Field Control Problems Department, State Institution "Institute of Technical Problems of Magnetism of the National Academy of Sciences of Ukraine", Kharkiv, Ukraine,
e-mail: kuznetsov.boris.i@gmail.com, ORCID: 0000-0002-1100-095X.

Tatyana Nikitina – D.Sc. in Engineering, Professor, Head of Sciences and Humanities Department, Kharkiv National Automobile and Highway University, Kharkiv, Ukraine,
e-mail: tatjana5555@gmail.com, ORCID: 0000-0002-9826-1123.